Inorganic Chemistry

pubs.acs.org/IC Article

Installing Quinol Proton/Electron Mediators onto Non-Heme Iron Complexes Enables Them to Electrocatalytically Reduce O₂ to H₂O at High Rates and Low Overpotentials

Segun V. Obisesan, Maksuda Parvin, Matthew Tao, Eric Ramos, Alexander C. Saunders, Byron H. Farnum,* and Christian R. Goldsmith*



Cite This: Inorg. Chem. 2024, 63, 14126-14141



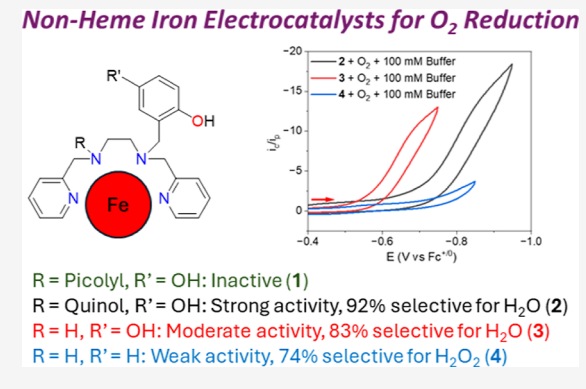
ACCESS I

III Metrics & More

Article Recommendations

3 Supporting Information

ABSTRACT: We prepare iron(II) and iron(III) complexes with polydentate ligands that contain quinols, which can act as electron proton transfer mediators. Although the iron(II) complex with N-(2,5-dihydroxybenzyl)-N,N',N'-tris(2-pyridinylmethyl)-1,2-ethanediamine (H_2 qp1) is inactive as an electrocatalyst, iron complexes with N,N'-bis(2,5-dihydroxybenzyl)-N,N'-bis(2-pyridinylmethyl)-1,2-ethanediamine (H_4 qp2) and N-(2,5-dihydroxybenzyl)-N,N'-bis(2-pyridinylmethyl)-1,2-ethanediamine (H_2 qp3) were found to be much more active and more selective for water production than a previously reported cobalt- H_2 qp1 electrocatalyst while operating at low overpotentials. The catalysts with H_2 qp3 can enter the catalytic cycle as either Fe(II) or Fe(III) species; entering the cycle through Fe(III) lowers the effective overpotential. On the basis of their TOF0 values, the successful iron—quinol complexes are



better electrocatalysts for oxygen reduction than previously reported iron-porphyrin compounds, with the $Fe(III)-H_2qp3$ arguably being the best homogeneous electrocatalyst for this reaction. With iron, the quinol-for-phenol substitution shifts the product selectivity from H_2O_2 to water with little impact on the overpotential, but unlike cobalt, this substitution also greatly improves the activity, as assessed by TOF_{max} , by hastening the protonation and oxygen binding steps. The addition of a second quinol further enhances the activity and selectivity for water but modestly increases the effective overpotential.

■ INTRODUCTION

The oxygen reduction reaction (ORR) is integral to the operation of hydrogen fuel cells and metal air batteries; in both devices, O₂ is reduced to H₂O through the addition of 4e⁻ and 4 protons. O2 can also be partially reduced to H2O2 through the net addition of 2e⁻ and 2 protons. For energy applications, this second reaction is problematic in that H_2O_2 can oxidatively damage parts of fuel cells and batteries. Reactions that selectively convert O_2 to H_2O_2 are nonetheless valuable, however, since H2O2 is an important feedstock for several industrial processes. Consequently, understanding the factors that influence an electrocatalyst's selectivity for one product over the other could provide great benefits.2 Although platinum-containing materials can be highly efficient and water-selective ORR electrocatalysts in fuel cell cathodes, the high cost and low natural abundance of platinum severely limit the widespread production of devices that rely on this element. This has motivated efforts to develop catalysts that use more economical and sustainable alternatives, such as first-row transition metals.^{2,3}

Metalloenzymes, such as cytochrome c oxidase and cytochrome P450, demonstrate that first row transition metals can indeed efficiently activate O_2 . Heme enzymes, in

particular, have inspired a variety of homogeneous and heterogeneous electrocatalysts for ORR consisting of first-row transition metals and either porphyrin, corrole, or phthalocyanine ligands. $^{10-21}$ Although most of these electrocatalysts are highly selective for the four electron reduction of $\rm O_2$ to $\rm H_2O$, they require effective overpotentials that are likely too high for practical use. 22 Cobalt complexes with porphyrin, corrole, and phthalocyanine ligands tend to have lower overpotentials but slower activity and lesser selectivity for $\rm H_2O$ than their iron-containing analogs. $^{23-27}$

First-row transition metal complexes with nonporphyrinic ligands have also been investigated as catalysts for ORR. These tend to function at lower overpotentials but generally yield $\rm H_2O_2$ as the major product. In addition, most of these ORR reactions have also been studied using chemical

Received: May 13, 2024 Revised: June 10, 2024 Accepted: July 9, 2024 Published: July 15, 2024





reductants rather than a current. Wang et al. used cobalt complexes with linear ligands with N2O2 donor sets to catalyze the reduction of O₂ to H₂O₂ using decamethylferrocene (Fc*) as a chemical reductant; the overpotentials for these catalysts were estimated to be as low as 90 mV.²⁸ Nichols et al. developed a cobalt complex with a related N2O2 ligand that was instead selective for H2O production from O2; the overpotential, however, was much higher (1.24 V).²⁹ The ORR with Nichols's complex can be made more selective for H₂O₂ with the installation of two pendent methoxy groups.³⁰ It was proposed that the installed alkoxy groups favor H2O2 release by relaying protons to the proximal O atoms of metal bound hydroperoxides. Wang et al. proposed a similar underlying rationale for the H₂O₂ selectivity of their systems.³¹ In two separate reports, Cook et al. selectively reduced O2 to H2O using iron complexes with N₃O donor sets. ^{32,33} In each case, the O₂ is reduced through two sequential 2e⁻ steps, with H₂O₂ as an intermediate. The overpotentials are believed to be low, but the authors cautioned that they were unable to measure these accurately since catalysis was only observed when a nonbuffered acid source was used.3

The product selectivities of the nonheme catalysts can be modestly shifted toward H₂O by introducing electron proton transfer mediator (EPTM) additives. Anson and Stahl first demonstrated that free 1,4-hydroquinone (quinol) could alter the ORR product distribution with cobalt-salophen catalysts.³⁸ Hooe et al. subsequently used quinol to improve the H₂O selectivity of a manganese-salen electrocatalyst for ORR. 40 In our previous work, we determined that covalently attaching quinol groups to pyridylamine ligands could impact the electrocatalytic activities of their Co(II) complexes. 41 The Co(II) complex with N,N,N'-tris(2-pyridinylmethyl)-1,2-ethanediamine (trispicen) could not act as an electrocatalyst for ORR. Adding a phenol to the secondary amine in the ligand yielded a catalyst that operated at a 0.31 V overpotential but was selective for H₂O₂. Incorporating a quinol, however (H₂qp1, Scheme 1), resulted in an electrocatalyst that was

Scheme 1. Structures of the Polydentate Ligands and Formulae of the Fe(II) and Fe(III) Complexes Relevant to This Study

instead selective for H_2O while operating at a nearly identical overpotential (0.33 V). The major drawback associated with the cobalt- H_2 qp1 complex was that its activity is relatively low, with a turnover frequency (TOF) of 0.154 s⁻¹. With homogeneous electrocatalysts for ORR, the TOF generally increases with higher overpotentials. ^{23,42} Dinda et al. found

that appending quinol groups to the salophen framework likewise greatly shifted the product selectivity of cobalt-containing electrocatalysts from H_2O to H_2O_2 ; their complex differs from ours in that the quinols are not in a position to coordinate to the metal center.⁴³

Given that iron-for-cobalt substitutions resulted in higher activity and selectivity for H_2O for porphyrin-, corrole-, and phthalocyanine-containing homogeneous electrocatalysts for ORR, we decided to investigate iron complexes with quinol-containing ligands (Scheme 1). Although the iron complex with H_2 qp1 was inactive as a catalyst, Fe(II) and Fe(III) complexes with two other quinol-containing ligands are highly active and water-selective electrocatalysts for ORR despite their low overpotentials.

■ EXPERIMENTAL SECTION

Materials. Except where stated otherwise, all chemicals and solvents were purchased from Sigma-Aldrich and used as received. Iron(II) triflate and iron(III) triflate were bought from Sigma-Aldrich. Ferrocene (Fc, 99%) was bought from Alfa Aesar, purified via sublimation, and stored under an inert atmosphere until immediately prior to use. Tetrabutylammonium hexafluorophosphate ([Bu₄N]-[PF₆], TBAPF₆) was recrystallized twice from ethanol and dried in an 80 °C oven until used. N-(2,5-Dihydroxybenzyl)-N,N',N'-tris(2-pyridinylmethyl)-1,2-ethanediamine (H₂qp1), N,N'-bis(2,5-dihydroxybenzyl)-N,N'-bis(2-pyridinylmethyl)-1,2-ethanediamine (H₄qp2), and N-(2,5-dihydroxybenzyl)-N,N'-bis(2-pyridinylmethyl)-1,2-ethanediamine (H₂qp3) were synthesized as previously described. 44,45

Instrumentation. All ¹H NMR data were obtained on a 500 MHz AV Bruker NMR spectrometer. All reported resonance frequencies were referenced relative to internal standards. High-resolution mass spectrometry data were acquired at the Mass Spectrometer Center at Auburn University on a Bruker microflex LT mass spectrometer. A Johnson Matthey magnetic susceptibility balance (model MK I#7967) was used to measure the magnetic moments of solid-state paramagnetic metal complexes. A Thermo Scientific iS-50 FTIR Spectrophotometer was used to collect IR data. UV/vis data were taken using a Varian Cary 50 spectrophotometer and processed using software from the WinUV Analysis Suite. Solid samples of isolated Fe(II) and Fe(III) complexes were dried under vacuum, stored under N₂, and sent to Atlantic Microlabs (Norcross, GA) for elemental analysis.

Cyclic Voltammetry. Cyclic voltammetry (CV) was performed using a Pine WaveDriver bipotentiostat using a 3 mm glassy carbon working electrode that was polished between each experiment, a Pt wire counter electrode, and a nonaqueous Ag+/Ag pseudoreference electrode. Samples were analyzed in a 20 mL electrochemical glass cell with a Teflon cell top purchased from BASi Inc. In CV experiments where O_2 was present, O_2 gas was sparged into the glass cell containing solutions of the electrocatalyst stirred at 300 rpm for 15 min prior to data collection. Solutions for anaerobic CV experiments were degassed by sparging with N2 for 30 min. At the end of each measurement, Fc was added to the solution, and an additional CV scan was taken to measure the Fc+/Fc (Fc+/0) potential to calibrate the Ag⁺/Ag potentials for the organic solvent. 46 Unless stated otherwise, all CV scans were conducted at a scan rate of 100 mV/s at 293 K. The maximum concentration of O2 in MeCN solutions containing 100 mM TBAPF₆ was previously determined to be 6.3 mM.47

Internal resistance was minimized by reducing the distance between the working and the reference electrode and corrected during each experiment by measuring the solution resistance using chronoamperometry at an applied potential which produces only nonfaradaic current.

Rotating Ring Disk Voltammetry Measurements. Rotating ring disk electrode (RRDE) data were collected using a Pine Instrument bipotentiostat and a Pine Instrument rotator with a 5 mm glassy carbon disk electrode, a coiled Pt wire secondary working

electrode, and a Ag⁺/Ag pseudoreference electrode. Solutions were analyzed in a custom-built 50 mL four-necked glass cell. Prior to each experiment, the electrochemical cell was thoroughly rinsed with acetonitrile (MeCN), water, and acetone. After the rinses, the cell was dried and stored in a 120 °C vacuum oven until immediately prior to use. The glassy carbon disc and Pt ring were polished vigorously with a Buehler felt pad between each RRDE scan to ensure the reproducibility of collected data. The collection efficiency (N) was determined by analyzing Fc in MeCN under N₂ and was calculated to be 0.34, based on the observed $-i_{\rm ring}/i_{\rm disc}^{48}$

For each experiment, 1.0 mM of the electrocatalyst was dissolved in 50 mL of degassed MeCN containing 100 mM TBAPF₆. The disc was scanned from -100 to -1000 mV vs Fc^{+/0} at 10 mV/s while the potential of the ring was set at +850 mV vs Fc⁺/Fc. Since a buffered source of acetic acid (AcOH) was used, background oxidation of the buffer was observed at potentials greater than +750 mV vs Fc⁺/Fc. Since this increased the magnitude of the ring currents, RRDE data collected under N₂ were subtracted from those collected under O₂ to get corrected ring and disc currents. RRDE scans were collected at 400, 900, 1600, and 2500 rpm. The corrected disc currents ($i_{\rm disc}$) and ring currents ($i_{\rm ring}$) were used to calculate the number of electrons involved in the catalytic process (n) using eq 1.⁴⁰ In eq 2, p is the fraction of H₂O₂ in the products of oxygen reduction. The Faradaic efficiency (FE) for H₂O₂, which is equivalent to the percent selectivity for H₂O₂, was determined using eqs 2 and 3.⁴

$$n = 4 \times \frac{i_{\rm disc}}{(i_{\rm disc} + i_{\rm ring})/N} \tag{1}$$

$$p = n - 2 \tag{2}$$

FE or
$$\% \text{ H}_2\text{O}_2 = p \times 100$$
 (3)

Spectrochemical Determination of Selectivity. The formation of H_2O_2 from O_2 was also spectrophotometrically monitored using titanium(IV) oxysulfate, $[\mathrm{Ti}^{IV}(\mathsf{O})\mathrm{SO}_4]$. ^{38,49} For this analysis, we first established a calibration curve by adding various concentrations of urea $\cdot H_2O_2$ to the $\mathrm{Ti}(\mathrm{IV})$ complex and measuring the absorbance at 409 nm. To determine the selectivities of catalysts for producing H_2O_2 from O_2 and a chemical reductant, we dissolved 0.2 mM catalyst, 1.0 mM decamethylferrocene, and 100 mM AcOH in 10 mL of MeCN under N_2 . After the reagents were mixed, O_2 was sparged into the stirred solution for 75 min. Aliquots of the reaction mixture were collected at various time points and diluted with an equal volume of MeCN. The UV/vis spectra before and after the addition of $[\mathrm{Ti}^{\mathrm{IV}}(\mathrm{O})\mathrm{SO}_4]$ were measured. We used eq 4 to quantify the selectivity.

$$\% H2O2 = \frac{[H2O2]}{2[decamethylferrocene]} \times 100$$
 (4)

Determination of k_{obs} . After the selectivity for the products was determined, observed rate constants (k_{obs}) were obtained using variable scan rate data and eq 5.50,51 In eq 5, n is the number of electrons transferred under catalytic conditions, i_{c} is the current under catalytic conditions, i_{p} is current in the absence of substrate, R is the gas constant, T is the temperature (293 K), v is the scan rate, and F is the Faraday constant. We define the k_{obs} as being equal to the maximum TOF (TOF_{max}) for a particular set of conditions. We explored using a foot of the wave analysis (FOWA)⁵⁰ to obtain k_{obs} values, but FOWA was not suitable for 2, 3, and 4 due to the nonlinearity of their plots. This suggests that the first chemical step is not the sole rate-determining step (RDS) for these electrocatalysts. ⁵¹

$$\frac{i_{\rm c}}{i_{\rm p}} = \frac{n}{0.4463} \sqrt{\frac{RTk_{\rm obs}}{F\nu}} \tag{5}$$

The n used in eq 5 is the weighted average of the number of electrons per catalytic process (eq 6), where $FE(H_2O) = 100\% - FE(H_2O_2)$. The k_{obs} values correspond to the consumption of O_2 and is a weighted mixture of the observed rate constants for the individual reactions that produce H_2O and H_2O_2 .

$$n = [4 \times FE(H_2O)] + [2 \times FE(H_2O_2)]$$
 (6)

Determination of Effective Overpotential. Effective overpotentials ($\eta_{\rm eff}$) were estimated using eq 7, which was developed for homogeneous electrocatalysts for the ORR. 42 $E_{{\rm O}_2/{\rm H}_2{\rm O}}^{\circ}$ is the standard equilibrium potential for ${\rm O}_2/{\rm H}_2{\rm O}$ under buffered conditions in MeCN; we estimated this value to be -0.1957 V vs ${\rm Fc}^{+/0}$ using eq 8, which ignores contributions from adventitious ${\rm H}_2{\rm O}$.

$$\eta = E_{\rm O_2/H_2O}^{\circ} - E_{\rm cat/2} \tag{7}$$

$$E_{\text{O}_2/\text{H}_2\text{O}}^{\circ} = 1.21 \text{ V} - 0.0592 \text{pK}_{\text{a}} \text{ (HA)} + 2.303 \frac{RT}{nF}$$
 (8)

The p K_a of AcOH (HA) in MeCN is 23.5,⁵³ R is the gas constant, n is the number of electrons involved in the catalytic process, T is the temperature (293 K), and F is the Faraday constant.

Syntheses. *N-*(2-Hydroxybenzyl)-*N*,*N'*-bis(2-pyridinylmethyl)-1,2-ethanediamine (Hpp3). 2-Hydroxybenzaldehyde (0.552 g, 4.00 mmol) and bispicen (1.030 g, 4.25 mmol) were dissolved in 20 mL ether. The resultant mixture was stirred for 4 h, during which time a solid deposited. The precipitate was collected and washed with a mixture of MeOH/ether (1:9 v/v). The isolated and washed aminal (0.900 g, 2.48 mmol) was dried and redissolved in 30 mL of MeOH. Trifluoroacetic acid (0.750 g, 6.58 mmol) was added to the MeOH solution at 0 °C, followed by sodium cyanoborohydride (0.220 g, 3.50 mmol). The mixture was stirred at RT for 12 h before the solvent was removed to yield the crude product. The crude product was purified by precipitation from MeOH/ether to yield the product as a white solid (0.731 g, 49% yield). Typical yields range from 45 to 54%. IR (cm⁻¹): 3006 (w), 2940 (w), 2806 (m), 2594 (w), 1611 (w), 1588 (m), 1568 (m), 1514 (s), 1472 (m), 1432 (s), 1374 (m), 1300 (w), 1270 (w), 1244 (s), 1169 (w), 1147 (w), 1116 (m), 1093 (m), 1046 (s), 1007 (m), 995 (w), 972 (m), 897 (m), 870 (w), 852 (w), 825 (s), 769 (m), 754 (s), 734 (w), 718 (w), 642 (w), 626 (w), 607 (w), 573 (m), 525 (s), 499 (w), 472 (w), 451 (w). ¹H NMR (500 MHz, CD₃OD, 293 K): δ 8.63 (d, J = 4.5 Hz, 2H), 8.42 (d, J = 4.5 Hz, 1H), 7.78–7.90 (m, 2H), 7.53–7.38 (m, 6H), 7.1 (m, 1H), 6.7 (m 1H), 4.42 (s, 2H) 4.28 (s, 2H), 3.95 (s, 2H), 3.33 (m, 2H), 3.05 (m, 2H). 13 C NMR (125 MHz, CD₃OD, 293 K): δ 158.39, 151.50, 149.21, 148.25, 137.50, 137.31, 124.03, 123.53, 122.48, 117.44, 115.99, 115.13, 57.77, 49.61, 49.30, 44.66. MS (ESI): calcd for LH+, 349.2028; found, 349.2017.

(N-(2,5-Dihydroxybenzyl)-N,N',N'-tris(2-pyridinylmethyl)-1,2ethanediamine)iron(II) Triflate ($[Fe^{II}(H_2qp1)](OTf)_2$, 1). H_2qp1 (0.50) g, 1.00 mmol) and $Fe^{II}(OTf)_2$ (0.39 g, 1.00 mmol) were dissolved in 2.5 mL MeCN under N2 and stirred at RT. After 18 h, 2.5 mL ether was added to the solution to precipitate the crude product. The solid was further purified with an $\overline{MeCN}/ether~(1:5~v/v)$ wash and dried under N₂ to yield the product as a dark green powder (0.41 g, 51% yield). Typical yields range from 47 to 53%. Optical spectroscopy (MeCN, 294 K): 300 nm (8400 M⁻¹ cm⁻¹), 385 nm (7300 M⁻¹ cm⁻¹). IR (cm⁻¹): 3327 (m), 1606 (m), 1571 (w), 1444 (m), 1236 (m), 1221 (m), 1153 (m), 1072 (w), 1055 (w), 1026 (s), 944 (s), 820 (m), 759 (s), 633 (s), 572 (m), 515 (m). MS (ESI): calcd for [Fe(Hqp1)]+, 510.1592; found, 510.1584. Solid-state magnetic susceptibility (295 K): 4.7 $\mu_{\rm B}$. Elemental analysis: Calcd for C₂₉H₂₉N₅FeF₆O₈S₂·2H₂O·CH₃CN: C, 41.35%; H, 4.03%; N, 9.33%. Found: C, 41.70%; H, 4.08%; N, 9.39%.

(N,N'-Bis(2,5-dihydroxybenzyl)-N,N'-bis(2-pyridinylmethyl)-1,2-ethanediamine)iron(II) Triflate ([Fe^{II}(H₄qp2)](OTf)₂, 2). H₄qp2 (0.50 g, 1.00 mmol) and Fe^{II}(OTf)₂ (0.36 g, 1.00 mmol) were dissolved in 2.5 mL MeOH under N₂ and stirred at RT. After 18 h, 2.5 mL ether was added to the solution to precipitate the crude product. The solid was further purified with an MeOH/ether (1:5 v/v) wash and dried under N₂ to yield the product as a dark blue powder (0.46 g, 55% yield). Typical yields range from 55 to 64%. Optical spectroscopy (MeCN, 294 K): 302 nm (18,700 M⁻¹ cm⁻¹), 474 nm (1300 M⁻¹ cm⁻¹), 525 nm (830 M⁻¹ cm⁻¹). IR (cm⁻¹): 3368 (m), 2922 (w), 1606 (m), 1572 (w), 1484 (m), 1442 (m), 1219 (m), 1155 (m), 1090 (w), 1053 (m), 1023 (s), 986 (w), 940 (m), 868 (w), 811 (m), 761

(m), 719 (w), 633 (s), 572 (m), 555 (m), 514 (m). MS (ESI): calcd for [Fe(H₂qp2)]⁺, 540.1460; found, 540.1448. Solid-state magnetic susceptibility (295 K): 4.8 $\mu_{\rm B}$. Elemental analysis: Calcd for C₃₀H₃₀N₄FeF₆O₁₀S₂·2H₂O·CH₃OH: C, 40.36%; H, 4.15%; N, 6.07%. Found: C, 40.84%; H, 4.12%; N, 5.94%.

(N-(2,5-Dihydroxybenzyl)-N,N'-bis(2-pyridinylmethyl)-1,2ethanediamine)iron(II) Triflate ($[Fe^{II}(H_2qp3)](OTf)_2$, **3**). H_2qp3 (0.50) g, 1.00 mmol) and $\mathrm{Fe^{II}(OTf)_2}$ (0.48 g, 1.00 mmol) were dissolved in 2.5 mL MeCN under N2 and stirred at RT. After 18 h, 2.5 mL ether was added to the solution to precipitate the crude product. The solid was further purified with an MeCN/ether (1:5 v/v) wash and dried under N₂ to yield the product as a pale blue powder (0.28 g, 40% yield). Typical yields range from 36 to 42%. Optical spectroscopy (MeCN, 294 K): 305 nm (15,900 M⁻¹ cm⁻¹), 480 nm (1900 M⁻ cm⁻¹). IR (cm⁻¹): 3231 (m), 2028 (w), 1607 (w), 1483 (w), 1444 (w), 1377 (w), 1239 (m), 1222 (m), 1155 (s), 1053 (w), 1025 (s), 823 (w), 760 (m), 722 (w), 635 (s), 572 (w), 514 (m). MS (ESI): calcd for [Fe(Hqp3)]+, 418.1092; found, 418.1087. Solid-state magnetic susceptibility (295 K): 4.7 μ_B . Elemental analysis: Calcd for C₂₃H₂₄N₄FeF₆O₈S₂: C, 38.99%; H, 3.98%; N, 7.13%. Found: C, 38.70%; H, 4.08%; N, 7.09%.

(N-(4-Hydroxybenzyl)-N,N'-bis(2-pyridinylmethyl)-1,2ethanediamine)iron(II) Triflate ([Fe^{II}(Hpp3)](OTf)₂, 4). Hpp3 (0.35 g, 1.00 mmol) and Fe^{II}(OTf)₂ (0.35 g, 1.00 mmol) were dissolved in 2.5 mL MeCN under N2 and stirred at RT. After 18 h, 2.5 mL ether was added to the solution to precipitate the crude product which was purified with an MeCN/ether (1:5 v/v) wash and dried under N2 to yield the product as a blue powder (0.43 g, 58% yield). Typical yields range from 55 to 61%. Optical spectroscopy (MeCN, 294 K): 265 nm $(16,700 \text{ M}^{-1} \text{ cm}^{-1}), 362 \text{ nm} (4200 \text{ M}^{-1} \text{ cm}^{-1}), 610 \text{ nm} (2200 \text{ M}^{-1})$ cm⁻¹). IR (cm⁻¹): 3018 (m), 2814 (m), 2491 (w), 1663 (s), 1592 (s), 1503 (w), 1472 (w), 1456 (w) 1428 (m), 1367 (w), 1270 (w), 1197 (w), 1177 (m), 1133 (s), 1042 (m), 1020 (m), 998 (m), 973 (m), 963 (w), 902 (w), 837 (s), 803 (s), 792 (s), 768 (s), 748 (m), 722 (s), 632 (m), 618 (m), 599 (w), 515 (s), 468 (w), 441 (m). MS (ESI): calcd for [Fe(pp3)]+, 403.1221; found, 403.1168. Solid-state magnetic susceptibility (295 K): 4.8 $\mu_{\rm B}$. Elemental analysis: Calcd for $C_{23}H_{24}N_4FeF_6O_7S_2\cdot 2H_2O$: C, 36.72%; H, 3.75%; N, 7.45%. Found: C, 36.87%; H, 3.81%; N, 7.63%.

(N,N'-Bis(2,5-dihydroxybenzyl)-N,N'-bis(2-pyridinylmethyl)-1,2-ethanediamine)iron(III) Triflate ([Fe^{III}(H₄qp2)](OTf)₃, **2'**). H₄qp2 (0.50 g, 1.00 mmol) and Fe^{III}(OTf)₃ (0.70 g, 1.00 mmol) were dissolved in 2.5 mL MeOH under N₂ and stirred at RT. After 18 h, 2.5 mL ether was added to the solution to precipitate the crude product which was purified with a MeOH/ether (1:5 v/v) wash and dried under N₂ to yield the product as a pale blue powder (0.53 g, 54% yield). Typical yields range from 47 to 54%. Optical spectroscopy (MeCN, 294 K): 298 nm (22,500 M⁻¹ cm⁻¹), 464 nm (1600 M⁻¹ cm⁻¹). IR (cm⁻¹): 3295 (m), 1607 (m), 1564 (w), 1474 (w), 1441 (m), 1247 (w), 1220 (m), 1150 (s), 940 (w), 820 (m), 758 (s), 716 (w), 633 (s), 572 (m), 514 (s). Solid-state magnetic susceptibility (295 K): 5.7 μ_B. Elemental analysis: Calcd for C₃₁H₃₀N₄FeF₉O₁₃S₃·CH₃OH: C, 37.12%; H, 3.31%; N, 5.41%. Found: C, 37.70%; H, 3.38%; N, 5.47%.

(N-(2,5-Dihydroxybenzyl)-N,N'-bis(2-pyridinylmethyl)-1,2ethanediaminé)iron(ÍII)triflate ([Fe^{III}(H_2qp3)](OTf)₃, $\mathbf{3}'$). H_2qp3 (0.50 g, 1.00 mmol) and Fe^{III}(OTf)₃ (0.55 g, 1.00 mmol) were dissolved in 2.5 mL MeCN under N2 and stirred at RT. After 18 h, 2.5 mL ether was added to the solution to precipitate the crude product. The solid was washed with a solution of MeCN/ether (1:5 v/v) and dried under N₂ to yield the product as a pale blue powder (0.39 g, 45% yield). Typical yields range from 42 to 49%. Optical spectroscopy (MeCN, 294 K): 303 nm (15,300 M⁻¹ cm⁻¹), 480 nm (1100 M⁻ cm⁻¹). IR (cm⁻¹): 3350 (w), 1612 (m), 1507 (m), 1488 (m), 1449 (m), 1238 (m), 1220 (s), 1171 (m), 1089 (w), 1023 (s), 942 (w), 904 (w), 876 (w), 846 (w), 828 (m), 773 (m), 757 (s), 727 (w), 714 (w), 633 (s), 597 (w), 571 (m), 514 (s), 485 (w). Solid-state magnetic susceptibility (295 K): 5.8 $\mu_{\rm B}$. Elemental analysis: Calcd for $C_{24}H_{24}N_4FeF_9O_{11}S_3\cdot 0.5(C_2H_5)_2O: C, 31.63\%; H, 3.39\%; N, 5.90\%.$ Found: C, 31.48; H, 3.31%; N, 5.83%.

RESULTS

Synthesis and Characterization. The ligands H₂qp1, H_4qp2 , and H_2qp3 were synthesized through previously reported procedures. The phenolic analog of H_2qp3 , Hpp3, was synthesized by substituting 2-hydroxybenzaldehyde for 2,5-dihydroxybenzaldehyde in the reaction used to prepare H₂qp3 and was characterized through standard spectroscopic techniques (Figures S1-S4). The Fe(II) complexes 1, 2, 3, and 4 were synthesized by adding 1 equiv of Fe^{II}(OTf)₂ to H₂qp1, H₄qp2, H₂qp3, and Hpp3, respectively, in dry MeCN under N₂. The ligand structures and compositions of the iron complexes are provided in Scheme 1. The Fe(III) complexes 2' and 3' were prepared by reacting 1 equiv of Fe^{III}(OTf)₃ with 1 equiv of either H_4qp2 or H_2qp3 , respectively, in MeCN. Each Fe(II) and Fe(III) complex precipitates from solution upon the addition of dry ether. The solids were then washed with MeCN/ether and dried under vacuum to yield pure products. Complexes 2 and 2' were reprecipitated from MeOH/ether. The yields for the iron complexes were similar, ranging from 40% to 58%. The identities and purities of these compounds were confirmed by elemental analysis; attempts to obtain crystalline samples suitable for structural characterization have thus far been unsuccessful. All iron complexes were also characterized by mass spectrometry and IR and UV/ vis spectroscopies (Figures S5-S16 and 1). In MeCN, each

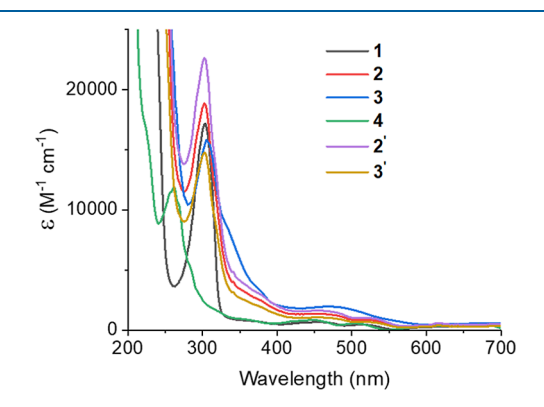
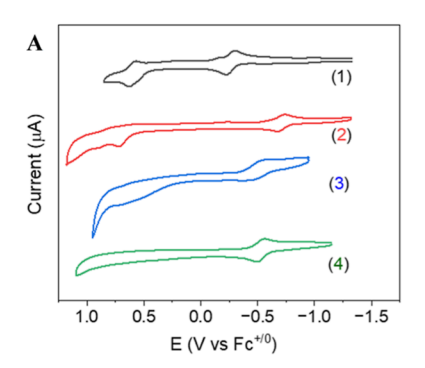


Figure 1. Comparative UV/vis spectra of the complexes described in this study. All data were taken from 0.050 mM samples of the complexes in 293 K MeCN with a 1.0 cm path length.

complex with a quinol-containing ligand absorbs strongly at ~ 300 nm (Figure 1). We have seen similar features for Mn(II), Zn(II), and Co(II) complexes with these ligands and attribute these bands to intraligand transitions within the quinols. ^{41,44,45,54,55} No bands are observed around 390 nm, suggesting that the quinols have not been deprotonated to quinolates. ^{56,57} The Fe(II) complex with the nonquinolic Hpp3 (4) lacks the band at ~ 300 nm. Magnetic susceptibility measurements are consistent with 1, 2, 3, and 4 each containing a S=2 high-spin Fe(II) metal ion. Complexes 2' and 3' have $\mu_{\rm eff}=5.7$ and 5.8 $\mu_{\rm B}$, respectively, consistent with mononuclear high-spin Fe(III) metal centers. Both 2' and 3' display EPR signals consistent with high-spin Fe(III) metal centers when analyzed at 4 K (Figure S17).

Electrochemistry of Iron Complexes under N_2 . CV studies of the complexes were performed in dry MeCN with 100 mM tetra-n-butyl ammonium hexafluorophosphate (TBAPF₆) as the supporting electrolyte.



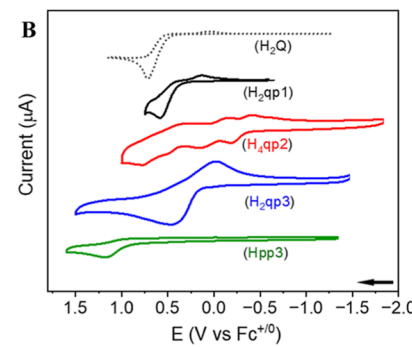


Figure 2. Full range CV scans for the iron complexes and their metal-free ligands. All data were taken in 293 K dry MeCN containing 100 mM TBAPF₆ under N₂. All scans began below -0.8 V vs Fc^{+/0} with initially increasing potential. All data are collected at a scan rate of 100 mV/s. (A) CV data for 1.0 mM 1, 2, 3, and 4. (B) CV data for 1.0 mM samples of the polydentate ligands used in this study and quinol (H₂Q).

In the absence of a proton source and O_2 , 1 displays a quasi-reversible redox feature with an $E_{1/2}$ of 0.61 V vs $Fc^{+/0}$, whereas 2 and 3 give rise to irreversible oxidation peaks at 0.71 and 0.65 V vs $Fc^{+/0}$, respectively (Figure 2). Since a redox event at a similar potential was observed for $[Co^{II}(H_2qp1)]^{2+}$, we assign the CV features seen for 1–3 to the oxidation of the quinols to para-quinones and when observed, their subsequent reduction to their original quinol forms. Complex 4 does not give rise to oxidation or reduction features around 0.65 V vs $Fc^{+/0}$, which is consistent with the compound lacking a quinol (Figure 2A). As anticipated, the data for the Fe(III) complexes 2' and 3' resemble those for 2 and 3 when analyzed in acetate buffer (Figure S18). Acetate by itself gives rise to an oxidation feature at about 1.0 V vs $Fc^{+/0}$, so but this gets shifted much more positive in the presence of acetic acid (Figure S18C).

We also analyzed the electrochemistry of quinol (H₂Q) and the free ligands under N₂ (Figure 2B). The organic compounds have redox features that are distinct from those of their Fe(II) complexes. The oxidation of H₂Q is irreversible in MeCN, with peak oxidation and reduction potentials of 0.72 V and -0.02 V vs Fc^{+/0}; these values are nearly identical to those measured by Hooe et al.⁵⁹ Similarly, the oxidation of H₂qp1 is irreversible, but the peak oxidation and reduction potentials shift to 0.57 and 0.11 V vs Fc^{+/0}, respectively. H₂qp3 has a redox feature with peak oxidation and reduction potentials that are nearly identical to those of H₂qp1 (0.57 and 0.13 V vs $Fc^{+/0}$). The diquinolic H_4qp2 ligand, on the other hand, has one irreversible and three quasi-reversible waves. That the data for this ligand appear much different than those of the others is likely a consequence of the second redox- and acid/base-active quinol. The oxidation features have peak potentials of -0.19, 0.14, 0.55, and 0.76 V vs $Fc^{+/0}$, whereas the reduction features appear at 0.33, -0.15, and -0.41 V vs Fc^{+/0}. Not surprisingly, the nonquinolic ligand Hpp3 looks much different than H₂Q and the quinolic ligands, having a single oxidation feature with a peak potential of 1.44 V vs $Fc^{+/0}$.

The potentials corresponding to the metal-associated redox processes vary more greatly than those of the ligand-derived ones, with 1 behaving much differently than the other iron complexes (Table 1). Under N_2 and in the absence of the buffer or an alternative proton source, 1 displays a reversible Fe(III/II) redox couple with $E_{1/2} = -0.26$ V vs Fc^{+/0} and $\Delta E_p = 60$ mV at a scan rate of 100 mV/s (Figures 2A and S19). Upon the addition of 1:1 acetic acid (AcOH)/tetrabutylammonium acetate (TBAA), we observe new reduction and oxidation features for 1 at -0.64 V and -0.32 vs Fc^{+/0}, respectively, which intensify as the buffer concentration

Table 1. Summary of Electrochemical Data for Fe(II) and Fe(III) Complexes with Quinol-Containing Ligands^a

complex	ligand redox (V vsFc ^{+/0})	$Fe(III/II) (E_{1/2}, V vsFc^{+/0})$
1	$0.64~(E_{\rm pa}),~0.58~(E_{\rm pc})$	-0.26
2	$0.71 \; (E_{\rm pa}), \; -0.25 \; (E_{\rm pc})$	-0.67
3	$0.65 (E_{pa})$	-0.56
4	N. A	-0.52
2'	$0.66~(E_{\rm pa}),~0.07~(E_{\rm pa}),~-0.21~(E_{\rm pc})$	-0.67
3′	$0.56 (E_{pa})$	-0.56

^aAll data were acquired in MeCN under N₂ with 100 mM TBAPF₆ as a supporting electrolyte and a 100 mV/s scan rate.

increases to 60 mM total acetate (Figure 3). As the buffer concentration is increased, new ligand-derived redox features

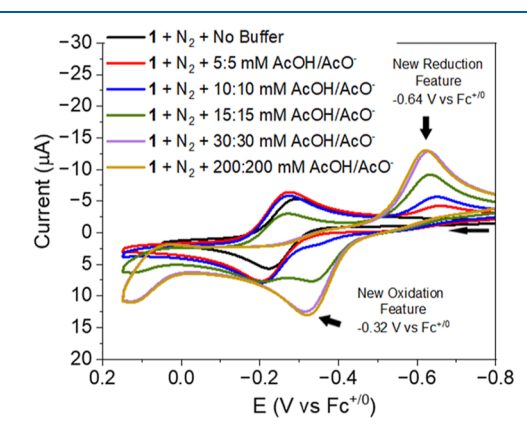


Figure 3. CV of 1.0 mM 1 under N_2 with increasing concentrations of acetate buffer (1:1 acetic acid/TBAA). 400 mM buffer contains 200 mM AcOH and 200 mM TBAA. All data are collected at a scan rate of 100 mV/s in dry MeCN at 293 K.

also appear at more negative values than those observed in the absence of buffer (Figure S20). The growth of these features with increased amounts of buffer suggests a pre-equilibrium to form a new species in the presence of buffer. This could be due to acetate coordination and/or deprotonation of the quinol. Furthermore, the increase in current for the redox waves centered near -0.5 V suggests two-electron reduction and oxidation, perhaps due to cooperative metal/ligand redox chemistry.

A quasi-reversible feature with a much more negative $E_{1/2}$ of -0.67 V vs Fc^{+/0} and $\Delta E_{\rm p} = 63$ mV is observed for 2 under an inert atmosphere in the absence of the buffer; this is assigned

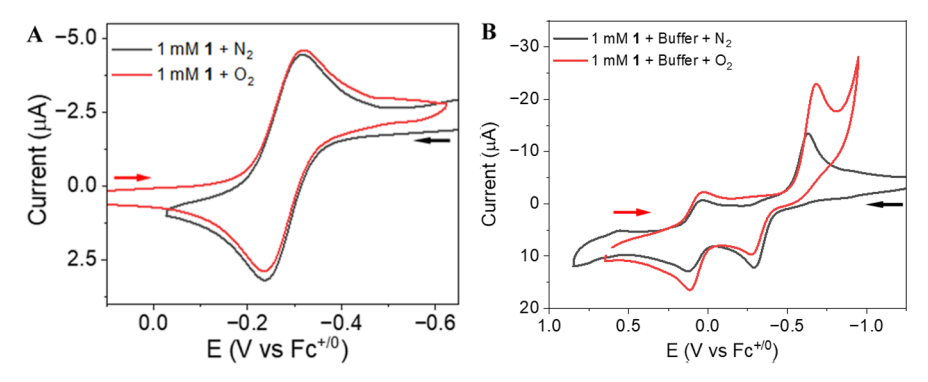


Figure 4. (A) CV of 1.0 mM 1 under N_2 and O_2 in MeCN. (B) CV of 1.0 mM 1 under N_2 and O_2 in MeCN with 400 mM acetate buffer (200 mM AcOH/200 mM TBAA). All data are collected at a scan rate of 100 mV/s at 293 K.

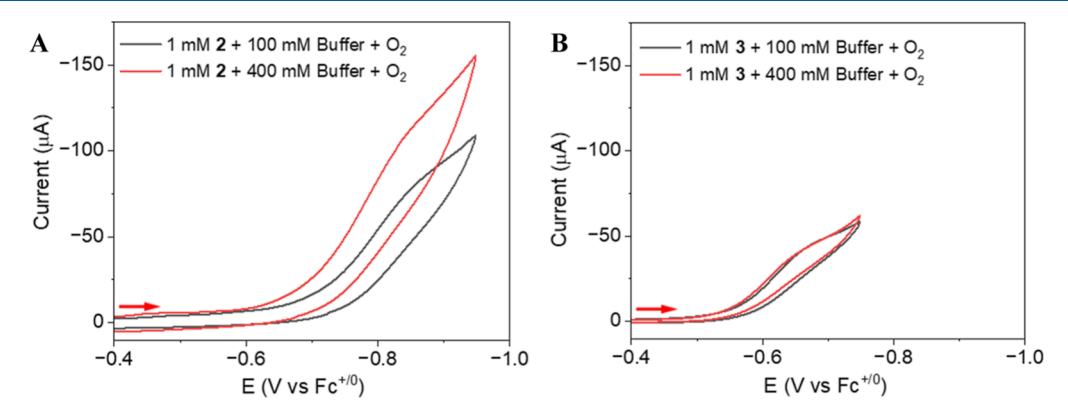


Figure 5. (A) CV of 1.0 mM 2 under O_2 with 100 and 400 mM acetate buffer. (B) CV of 1.0 mM 3 under O_2 with 100 and 400 mM acetate buffer. All data are collected at a scan rate of 100 mV/s in dry MeCN at 293 K.

to the Fe(III/II) couple (Figure 2A and S21). Titration of 2 with increasing concentrations of acetate buffer does not lead to any obvious changes to the $E_{1/2}$ of the metal-based redox feature, but it does shift the peak oxidation potential of the ligand-derived feature to a more negative value (Figure S22). Quasi-reversible Fe(III/II) features were also obtained for 3 and 4, with $E_{1/2}$ values of -0.56 V and -0.52 V vs $Fc^{+/0}$ respectively (Figures 2A, S23 and S24). These are again more negative than the one measured for 1. When the data are collected in 400 mM acetate buffer, the $E_{1/2}$ values for the Fe(III/II) features shift by -0.072 V for 3 and 0.021 V for 4 (Figures S25 and S26). The ligand-derived redox features observed for 3 also shift to more negative potentials, as they do for 1 and 2. The data suggest that the quinols in complexes 1-3 interact strongly with the buffer components, likely through hydrogen bonds. Similar cathodic shifts have been observed for the interaction between H₂Q (quinol) and acetate and have been attributed to the formation of quinol-acetate adducts as opposed to deprotonation of the quinol by the acetate.⁶⁰

Electrochemistry of Iron Complexes under O_2 . For 1, the Fe(III/II) redox feature remains reversible ($\Delta E_{\rm p} = 65$ mV) under O_2 in the absence of an external proton source (Figure 4A). Upon the addition of 400 mM acetate buffer (200 mM AcOH/200 mM TBAA), the current at the -0.64 V vs Fc^{+/0} reduction feature modestly increases in the presence of O_2 (Figure 4B). The increase in current is consistent with O_2 reduction; however, the lack of changes in the CV in unbuffered conditions suggest that O_2 reduction may be an outer-sphere process instead of an inner-sphere reduction where O_2 coordinates to the iron metal center. Furthermore, the continued presence of an anodic current for 1 near -0.3 V

suggests that the redox process retains some reversibility and thereby precludes us from definitively attributing the increase in the reduction current to electrocatalytic O_2 reduction. Further studies are underway to better understand the limited catalytic activity of 1.

When the diquinolic complex 2 is analyzed in O₂-saturated MeCN, the Fe(III/II) feature becomes irreversible with a concomitant increase in current even without a proton source (Figure S27), suggesting that O2 is coordinating to and being electrocatalytically reduced at the metal center. When the solution containing O2 and 2 is titrated with a buffered proton source, the catalytic current rises, scaling with the amount of acid added (Figures 5A and S28). Although most of the catalytic current can be correlated to solution-state electrocatalysis, we do observe background O_2 reduction at a potential of $-0.8~V~vs~Fc^{+/0}$. The contribution to the electrocatalysis is small, amounting to less than 10% of the total catalytic current. At potentials greater than -0.83 V vs Fc^{+/0}, however, the background O₂ reduction exceeds 10% and can no longer be considered negligible (Figure S29). Our findings are consistent with a small fraction of 2 adsorbing to the electrode and acting as a heterogeneous ORR electrocatalyst.

Like 2, 3 appears to bind to and electrocatalytically reduce O₂. When 3 is studied in O₂-saturated MeCN, the Fe(III/II) feature becomes irreversible with a concomitant rise in current (Figure S27). The current increases further as acetate buffer is introduced into the system (Figures SB and S30). Compound 3 differs from 2 in that the catalytic current does not indefinitely scale with the concentration of buffer. Instead, the current maximizes once the buffer concentration reaches 100

mM; higher buffer concentrations have no significant impact on the magnitude of the catalytic currents (Figures 5B and S30). Complex 3 also differs from 2 in that it overlaps less with the background O_2 reduction (Figure S31).

The phenolic analog to 3, complex 4, likewise displays a catalytic current in O_2 -saturated MeCN (Figure S32), but the weak magnitude of the catalytic current (i_c) relative to the noncatalytic current (i_p) prevents us from discerning its dependence on the concentration of buffer. Relative to 3 and 4, 2 appears to be more active, as indicated by the magnitudes of the catalytic currents with 100 mM acetate buffer (Figure 6).

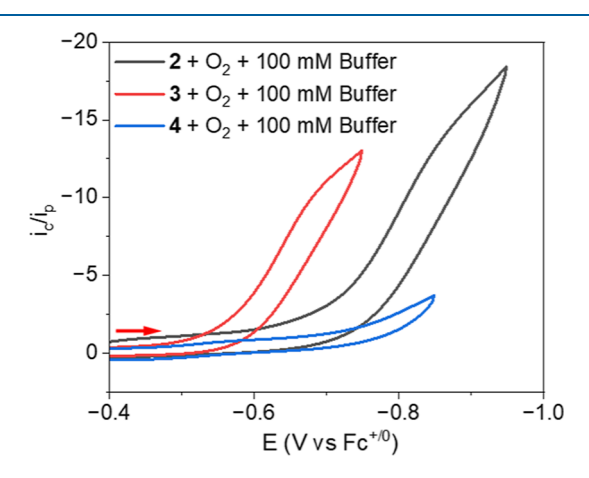


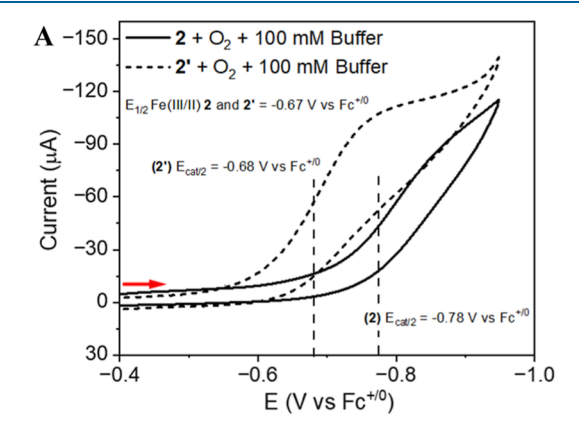
Figure 6. Comparative CV of 1.0 mM **2**, 1.0 mM **3**, and 1.0 mM **4** under O_2 with 100 mM acetate buffer. All reported potentials are vs Fc^+/Fc . All data are collected at a scan rate of 100 mV/s in dry MeCN with 100 mM acetate buffer (50 mM AcOH/50 mM TBAA) at 293 K. Catalytic current (i_c) was normalized to noncatalytic current (i_p).

Although the ferric compounds 2' and 3' generally behave like their Fe(II) analogs with regards to their electrochemical activity in the presence of O_2 , the Fe(II) and Fe(III) complexes differ with respect to their $E_{\rm cat/2}$ values. Complexes 2 and 3 have $E_{\rm cat/2}$ of -0.78 and -0.61 V vs Fc^{+/0}, respectively. The $E_{\rm cat/2}$ for 2' (-0.68 V vs Fc^{+/0}) and 3' (-0.56 V vs Fc^{+/0}) are noticeably less negative (Figure 7). The difference in the catalytic potentials for the Fe(II) (2, 3) and Fe(III) complexes (2', 3') likely results from the electrocatalysts entering the catalytic cycle through two distinct pathways. Much like 2, 2' appears to adhere to the electrode and engage in

heterogeneous electrocatalysis (Figure S33). The extent of adsorption, however, appears to be much more severe for 2', and this phenomenon limits our ability to analyze and assess its homogeneous electrocatalysis. We do not observe any noticeable electrode adsorption for 3' (Figure S34).

Selectivity, Effective Overpotentials and Maximum **Turnover Frequency.** The product selectivity, specifically the preference for H₂O or H₂O₂, was ascertained using two different methods: RRDE measurements and a colorimetric assay for H₂O₂ using Ti(O)SO₄. 38,49 Sometimes, electrocatalysts for ORR can react with and further reduce H2O2 to water. The RRDE measurements are less sensitive to these side reactions than the $Ti(O)SO_4$ assay and thereby tend to estimate higher yields of H_2O_2 . ³² Analysis of the RRDE data of the electrocatalysts in O2-saturated MeCN with 100 mM acetate buffer (Figures S35-S40) reveals that electrocatalytic ORR with 2 and 3 produces H_2O selectively: 92 \pm 3% (2), 83 \pm 5% (3). Catalyst 4, conversely, is more selective for H_2O_2 , which accounts for $74 \pm 6\%$ of its ORR products. The same general order is seen with the Ti(O)SO₄ assay (Figures S41-S44). Compounds 2 and 3 are over 98% and 94% selective for H₂O, respectively; whereas H₂O accounts for only 37% of the products from ORR catalyzed by 4. Compounds 2' and 3' are also selective for H₂O, with RRDE-determined selectivities of $89 \pm 4\%$ (2') and $81 \pm 3\%$ (3'). These values are identical within error to the analogous RRDE measurements for 2 and

The effective overpotentials $(\eta_{ ext{eff}})$ were determined using a modification of a literature protocol that was developed by the Mayer lab to analyze ORR.35 Since we could not obtain reversible or quasi-reversible Fe(III/II)-superoxide couples for **2**, **3**, and **4** under O_2 , we used $E_{\text{cat/2}}$ rather than the $E_{1/2}$ of the observed Fe(III/II) features. The Fe(III/II)-superoxide couples for these complexes should be much more negative than those of the observed metal-based features, as evidenced by the more negative onset potentials of 2 and 3 relative to 2' and 3'. The use of the Fe(III/II) $E_{1/2}$ values would therefore most likely underestimate the $\eta_{\rm eff}$ values of the reduced ORR electrocatalysts. Using this modified protocol and the estimated $-0.20~{\rm V}$ vs Fc^{+/0} $E^{\circ}_{{\rm O_2/H_2O}}$ (eq 8), the $\eta_{\rm eff}$ values for 2, 3, and 4 were calculated to be 0.58, 0.42, and 0.41 V, respectively. The overpotentials for 2' (0.48 V) and 3' (0.37 V) are both lower than those calculated for 2 and 3 due to their much more positive onset potentials. The differences in



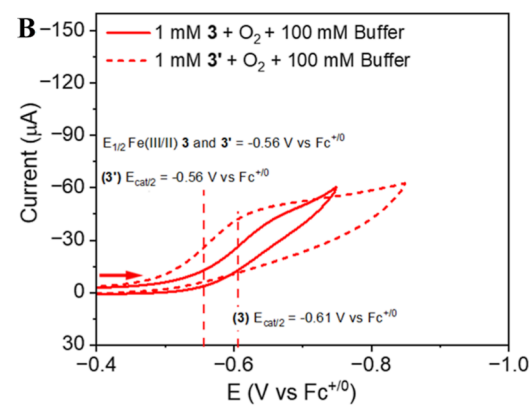


Figure 7. (A) Comparative CV of 1.0 mM 2 and 1.0 mM 2' under O_2 with 100 mM acetate buffer. (B) Comparative CV of 1.0 mM 3 and 1.0 mM 3' under O_2 with 100 mM acetate buffer. All reported potentials are vs Fc^+/Fc . All data are collected at a scan rate of 100 mV/s in dry MeCN at 293 K.

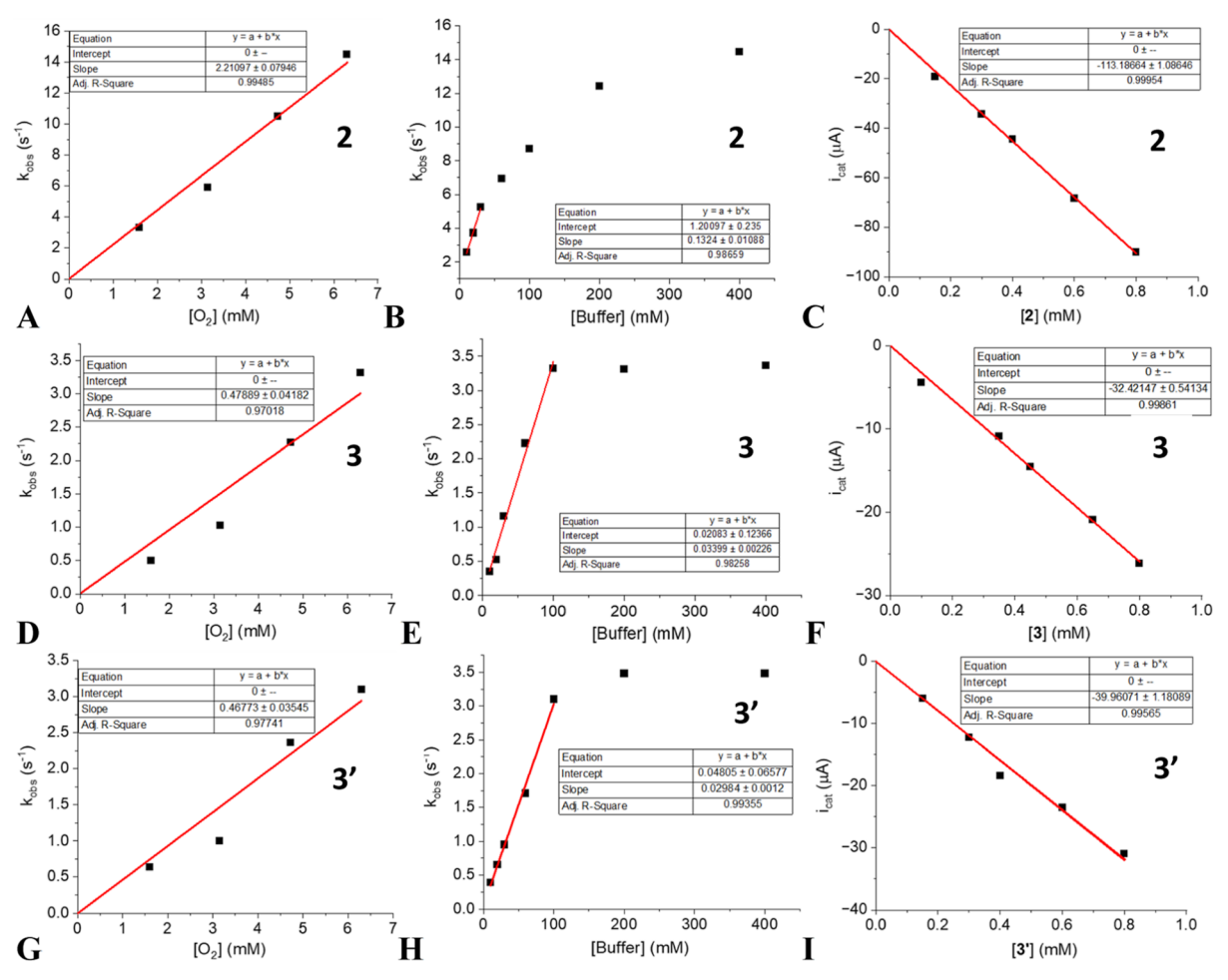


Figure 8. (A) Plot of k_{obs} vs $[O_2]$ for **2.** (B) Plot of k_{obs} vs [acetate] for **2.** (C) Plot of i_c vs $[\mathbf{2}]$. (D) Plot of k_{obs} vs $[O_2]$ for **3.** (E) Plot of k_{obs} vs [acetate] for **3.** (F) Plot of i_c vs $[\mathbf{3}]$. (G) Plot of k_{obs} vs $[O_2]$ for **3**'. (H) Plot of k_{obs} vs [acetate] for **3**'. (F) Plot of i_c vs $[\mathbf{3}']$. The listed buffer concentrations are the sums of the concentrations of AcOH and TBAA. The shown k_{obs} and i_c values are calculated from the data in Figures S28, S30, and S46–S49.

the overpotentials suggest that the reduced and oxidized complexes enter the catalytic pathway at different steps.

The maximum turnover frequencies (TOF_{max}) for **2**, **3**, and **3**' were obtained from CV data under conditions that resulted in the catalytic currents becoming independent of scan rate (Figure S45).⁶¹ The electrode adsorption observed for **2**' precludes us from measuring its TOF_{max}. These measurements estimate $k_{\rm obs}$ from the $i_{\rm c}/i_{\rm p}$ ratio and the $n_{\rm cat}$ determined from RRDE studies (vide infra), where $i_{\rm c}$ is the plateau catalytic current and $i_{\rm p}$ is the peak current for the electrocatalyst under N₂ (eq 5).⁶¹ The obtained $k_{\rm obs}$ values are estimated to be equal to the TOF_{max} values since the S-shaped catalytic currents are over 100 mV more negative than the E° of the catalysts. Attempts to corroborate these TOF_{max} values using FOWA were unsuccessful for **2**, **3**, and **3**' due to the curvatures of their slopes. ^{50,51}

We were unable to obtain scan rate-independent currents with 1.0 mM catalyst concentrations as we did for $[\text{Co}^{\text{II}}(\text{H}_2\text{qp1})]^{2+}$ and its phenolic analog. ⁴¹ Consequently, we analyzed 0.15 mM solutions of 2 and 3' and 0.10 mM solutions of 3 in order to obtain a larger excess of O_2 substrate relative to the catalysts. With these more dilute concentrations, we can obtain scan rate-independent currents from 100 to 150 mV/s for 2 and from 60 to 150 mV/s for 3. With 400 mM acetate buffer (200 mM AcOH/200 mM TBAA) and a 100

mV/s scan rate, we calculated TOF_{max} (k_{obs}) values of 14.6 s⁻¹ and 3.3 s⁻¹ for H₂O production by 2 and 3, respectively. The TOF_{max} was 3.2 s⁻¹ for 3', which was instead measured in 100 mM acetate buffer.

Determination of Reaction Rate Laws. To determine the rate laws for the electrocatalytic reactions, we correlated the measured $k_{\rm obs}$ values to the concentrations of ${\rm O_2}$ and buffered proton source. The concentration of ${\rm O_2}$ was controlled by combining portions from ${\rm O_2}$ -saturated and ${\rm O_2}$ -free solutions. Since scan rate-independent catalytic currents could be obtained, we could readily determine how the $k_{\rm obs}$ varied as a function of the ${\rm O_2}$ and buffer concentrations. For 2, 3, and 3', $i_{\rm c}$ scales linearly with the catalyst concentration, as expected for a first-order dependence of the rate on [2], [3], and [3'].

Using these methodologies, we find that with low concentrations of buffered acid, the rates are first-order with respect to substrate, acid, and catalyst for 2, 3, and 3' (Figures 8, S28, S30, S46–S49). We could not, however, accurately determine the reaction order for 1 and 4 since the catalytic currents, i_c , are much smaller and barely larger than the noncatalytic current i_p ; in the case of 1, the data do not clearly indicate any electrocatalytic O_2 activation by the iron complex.

The slopes and y-intercepts of the acid-dependent plots can approximate the rate constants for intermolecular and

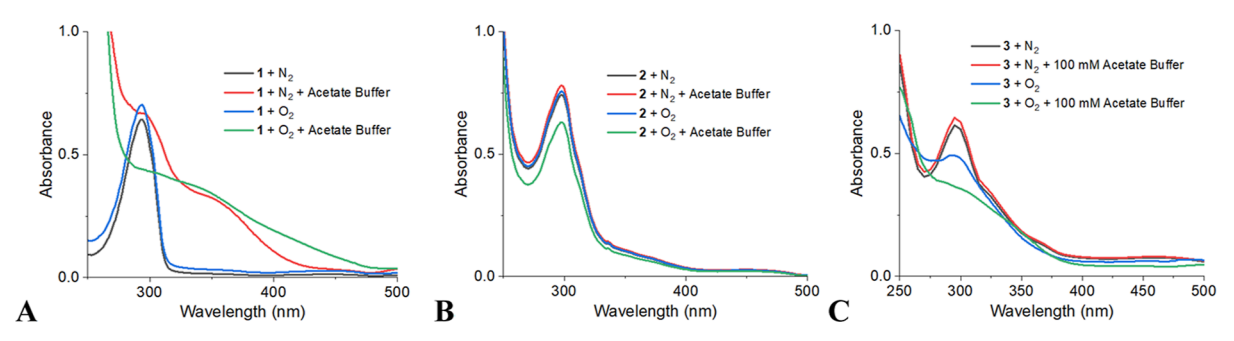


Figure 9. (A) Optical spectra of 0.05 mM 1 under N_2 and O_2 in the presence and absence of 100 mM acetate buffer (50 mM AcOH/50 mM NaOAc). (B) Optical spectra of 0.05 mM 2 under N_2 and O_2 in the presence and absence of 100 mM acetate buffer. (C) Optical spectra of 0.05 mM 3 under N_2 and O_2 in the presence and absence of 100 mM acetate buffer. All data were collected at 19 °C in MeCN with a 1.0 cm pathlength. Solutions of the iron complexes were sparged with O_2 for 3 h prior to data collection.

intramolecular protonation, respectively. The slopes are 130 M⁻¹ s⁻¹ (2), 34 M⁻¹ s⁻¹ (3), and 30 M⁻¹ s⁻¹ (3'); whereas the intercepts are 1.2 s⁻¹ (2), 0.021 s⁻¹ (3), and 0.048 s⁻¹ (3') (Figure 8B,D,H). Similar nonzero intercepts were observed for $[\text{Co}^{\text{II}}(\text{H}_2\text{qp1})]^{2+}$ and are consistent with the pendent quinol groups being able to both protonate and reduce O_2 in the absence of an external acid.⁴¹ At high concentrations of buffered acid, k_{obs} no longer scales linearly with the amount of acid and instead shows acid-independent behavior (Figure 8B,E,H). Analogous behavior was observed in several other reported molecular electrocatalysts for the ORR, including $[\text{Co}^{\text{II}}(\text{H}_2\text{qp1})]^{2+}$. ^{15-17,19,41}

The plots of $k_{\rm obs}$ vs $[{\rm O}_2]$ have slopes of 2200 M⁻¹ s⁻¹ (2), 480 M⁻¹ s⁻¹ (3), and 470 M⁻¹ s⁻¹ (3') (Figure 8A,D,G). These slopes are approximately equivalent to the rate constants for O₂ binding. Multiplying these values by the 6.3 mM concentration of O₂ used in the experiments with variable buffer concentrations yields first-order rate constants of 14 s⁻¹ (2), 3.0 s⁻¹ (3), and 3.0 s⁻¹ (3'); these are approximately equal to the $k_{\rm obs}$ values for the acid-independent portions of Figure 8B,E,H, suggesting that O₂ binding indeed becomes the RDS once the concentration of buffer reaches the threshold concentrations.

UV/Vis, ESI-MS, and EPR Studies of Non-Electrocatalytic Reactions with O_2 . Complexes 1, 2, and 3 were studied by UV/vis under N_2 and O_2 atmospheres at 19 °C (Figure 9). For 1, a single band at 298 nm is observed under N_2 and O_2 in the absence of an external proton source (Figure 9A). Upon the addition of acetate buffer, the intensity of this feature diminishes, and a new band develops at 366 nm when the sample is kept air-free. Under O_2 , the UV/vis spectrum of 1 likewise changes when acetate buffer is added; the 298 nm feature completely disappears.

With 2 and 3, conversely, the addition of acetate buffer does not alter the UV/vis spectrum under N_2 . Intense bands around 300 nm are found for both complexes in the buffered and unbuffered conditions; these are attributed to intraligand transitions for the quinolic portions of the ligand. When a solution of 2 is exposed to O_2 for 3 h in the absence of the buffer, the intensity of the band at 300 nm remains the same (Figure 9B). However, exposing 2 to O_2 in the presence of 100 mM acetate buffer noticeably weakens the feature. Adding O_2 to 3 results in more drastic decreases to the 300 nm band, and 3 differs from 2 in that a noticeable reaction with O_2 occurs even in the absence of acetate buffer (Figure 9C). The loss of the 300 nm feature would be consistent with the quinols of the ligand being oxidized to *para*-quinones. 44,45,57

The buffer-induced UV/vis changes that we observe for 1 under N_2 are consistent with the deprotonation of the quinol to a quinolate rather than the coordination of acetate. ⁴⁵ The inability of the buffer to deprotonate 2 and 3 to detectable extents suggests that 1 is noticeably more acidic than both 2 and 3. Direct titration of 1–3 with acetate confirms that 1 is more acidic (Figure S50).

ESI-MS data provide further insight into the reactivity of the Fe(II) complexes with O2 in the presence of acetate buffer (Figure S51). All three complexes oxidize to Fe(III) species upon reaction with O_2 ; these reactions either require (1) or are accelerated by the buffer (2, 3). The ease of oxidation scales with the $E_{1/2}$ of the Fe(III/II) couple, with 1 and 2 being the least and most reactive, respectively. The most prominent m/zfeature for 1 under N2 without acetate buffer corresponds to the ferrous complex with the singly deprotonated ligand, $[Fe^{II}(Hqp1)]^+$, which has a m/z = 510.1578 (calculated m/z =510.1592). A much smaller m/z feature at 255.0801 corresponds to the ferric complex with the singly deprotonated ligand, $[Fe^{III}(Hqp1)]^{2+}$ (calculated m/z = 255.0796). The data change only slightly upon 1 h exposure to O2 in pure MeCN, but the ferric feature becomes much more intense when the data are acquired for an aerobic sample with 100 mM acetate buffer (Figure S51C). For 2, the most readily identifiable m/zfeatures under N2 and O2 correspond to the ferric complex with the doubly deprotonated ligand, [Fe^{III}(H₂qp2)]⁺ (Figure S51D); the m/z ratio for the most diagnostic peak is 540.1448 (calculated m/z = 540.1460). The ferrous complex likely spontaneously oxidizes to the ferric species under the MS ionizing conditions. This observation is consistent with the Fe(II) oxidation state being much less stable for 2 than it is for the monoquinol complexes 1 and 3. In the MS data for 3 under N₂ (Figure S51G), we observe $[Fe^{II}(H_2qp3)]^{2+}$ at m/z =210.0587 (calculated m/z = 210.0624) and $[Fe^{III}(qp3)]^+$ at m/z = 210.0624z = 418.1087 (calculated m/z = 418.1092). Upon 1 h exposure to O₂ (Figure S51H), the ferrous peak shrinks and the intensity of the ferric peak increases. Furthermore, we observe additional Fe(III) species, notably the complex with the singly deprotonated ligand $[Fe^{III}(Hqp3)]^{2+}$ at m/z = 209.5580(calculated m/z = 209.5585) and the hydroxide complex $[Fe^{III}(Hqp3)(OH)]^+$ at m/z = 436.1179 (calculated m/z = 436.1179) 436.1198).

The reactions between all three Fe(II) complexes and O_2 in buffered MeCN yield additional products that have m/z features that cannot be readily assigned; these likely correspond to decomposition products. Overall, the data suggest that the O_2 reactions yield species that degrade in the

absence of a reductant. Due to its lesser reactivity with O_2 , we observe fewer decomposition features for 1.

The 77 K EPR spectra of 1, 2, and 3 in the absence of O_2 are essentially featureless, as anticipated for high-spin Fe(II) complexes (Figures S52–S54). Upon exposure to O_2 , signals at $g \sim 4.2$ appear for all three compounds; these correspond to rhombic high-spin Fe(III) species. We also observe low-spin Fe(III) species for each complex. For 2 and 3, these are trace features that are barely distinguishable from noise, with g values of 1.98 (2) and 1.97 (3). The low-spin Fe(III) signal for 1, however, is much more intense; its low-spin species has three g values at 2.21, 2.14, and 1.97 (Figure S52). The data are consistent with the H_2 qp1 ligand providing a stronger crystal field than either H_4 qp2 or H_2 qp3.

DISCUSSION

Previously, we found that installing a 1,4-hydroquinone (quinol) into a pyridylamine ligand enabled a cobalt compound that was previously electrocatalytically inactive to serve as an electrocatalyst for the ORR. ⁴¹ In work from other research groups, quinol was used as an EPTM additive for the ORR and improved the selectivity for $4e^-$ reduction of O_2 to water in two different studies. ^{38,40} The Co(II) complex with H_2 qp1 (Scheme 1) was slightly selective for the $4e^-$ reduction of O_2 , making water in a 61% yield. ⁴¹ An analog of the H_2 qp1 ligand that contains a phenol in place of the quinol (Hpp1, Scheme 2) likewise enabled electrocatalytic ORR with cobalt,

Scheme 2. Previously Prepared Phenolic and Quinolic Ligands

but the catalyst instead favored the $2e^-$ reduction of O_2 to H_2O_2 . Given the prevalence of iron in small molecule electrocatalysis of the ORR, $^{10-13,15-19,24,32,33,36}$ we decided to explore Fe(II) and Fe(III) complexes with H_2 qp1 and similar ligands for this activity.

In addition to H_2qp1 , we studied complexes with two additional quinol-containing ligands: H_4qp2 and H_2qp3 (Scheme 1). H_4qp2 contains a second quinol in place of one of the H_2qp1 pyridines. H_2qp3 is a monoquinol ligand that lacks one of the H_2qp1 picolyl arms; the compound differs from H_2qp1 and H_4qp2 in that it is at most pentadentate, rather than hexadentate. We considered including Hpp1 (Scheme 2) but discontinued its study once the Fe(II) complex with H_2qp1 was found to be catalytically inactive (vide infra). We instead studied the phenolic analog of H_2qp3 (Hpp3, Scheme 1). We had previously prepared an Fe(II) complex with the macrocyclic ligand H_4qp4 (Scheme 2). So The reactivity of the H_4qp4 compound with O_2 was found to

be sluggish, however, and our initial activity screens showed no electrocatalytic behavior.

The syntheses of the Fe(II) complexes with H_2qp1 (1), H_4qp2 (2), H_2qp3 (3), and Hpp3 (4) are straightforward, and we can obtain moderate yields of each compound from reactions between the ligands and $Fe^{II}(OTf)$ in MeCN. The complexes are generally hygroscopic and much more oxygen sensitive than both their Mn(II) analogs and the $Fe(II)-H_4qp4$ complex. 44,45,56 Dry MeCN and an anaerobic atmosphere are therefore essential to obtaining pure products. We also prepared Fe(III) complexes with H_4qp2 (2') and H_2qp3 (3') from the ligands and $Fe^{III}(OTf)_3$.

The changes to the ligand structure have a strong impact on the Fe(III/II) reduction potential in anaerobic MeCN (Figure 2 and Table 1). Among the quinol-containing complexes, I has the most positive potential ($-0.26~V~vs~Fc^{+/0}$), followed by 3 ($-0.56~V~vs~Fc^{+/0}$), then 2 ($-0.67~V~vs~Fc^{+/0}$). Relative to H₄qp2 and H₂qp3, the H₂qp1 ligand provides an extra pyridine donor; pyridines and their derivatives (e.g., phen, bipy) have been documented to make Fe(III/II) potentials more positive. The potentials for 3 and 4 ($-0.52~V~vs~Fc^{+/0}$) are nearly identical, which is consistent with the H₂qp3 and Hpp3 ligands providing essentially the same set of donor atoms. As anticipated, the Fe(III/II) potentials for the Fe(III) complexes 2' and 3' resemble those for 2 and 3.

Our data suggest that 1 is substantially more acidic than 2, 3, and 4, demonstrating that the quinol in the H₂qp1 ligand has a stronger affinity for the metal center. We propose that the additional pyridine in H₂qp1 enables it to provide a strongerfield coordination environment than the H₄qp2 and H₂qp3 ligands. This would increase the metal-ligand bond covalency and lower the pK_a values of metal-coordinated quinols. Our EPR data support this argument. When 1-3 are oxidized by O₂, 1 gives rise to a low-spin Fe(III) signal (Figure S52); 2 and 3, conversely, are converted to almost exclusively high-spin Fe(III) species (Figures S53 and S54). The coordination environments for 2, 3, and 4 are more ambiguous than that for 1. The N-donors of the ligands likely bond to the Fe(II) with the remaining coordination sites occupied by solvent molecules and loosely bound quinols. As far as their acid/ base properties are concerned, the pK_a of the phenolic O-H bond is equal within error to that of the first pK_a of quinol (9.9) in water).

Throughout our electrochemical studies, we use acetate buffer (1:1 acetic acid/tetrabutylammonium acetate) as a source of protons. The addition of this buffer has no impact on the Fe(III/II) potential of **2** and a near negligible influence on the Fe(III/II) potentials for **3** and **4**. With **1**, however, the metal-centered reduction becomes much less favorable (Figure 3). The reaction between **1** and acetate appears to deprotonate the quinol, as evidenced by UV/vis. The negatively charged quinolate renders the oxidation of both the iron and the ligand more favorable. We do not fully understand why we did not observe buffer-induced deprotonation with $[Co^{II}(H_2qp1)]^{2+}$ (5). Iron is generally considered to be slightly more oxophilic than cobalt, which leads to slightly higher pK_a values for Co(II)-O-H bonds. This may explain why **1** seems to be more acidic than its Co(II) analog.

Upon saturating their MeCN solutions with O_2 , the current at the Fe(III/II) reduction potential increases for $\mathbf{2}$, $\mathbf{3}$, and $\mathbf{4}$. The addition of O_2 also causes the metal-based redox features of these three complexes to become irreversible. For $\mathbf{2}$ and $\mathbf{3}$, the currents further increase upon the addition of a buffered

proton source. Although **2**, **3**, and to a much lesser extent **4** can bind to O_2 and subsequently reduce it, **1** is unable to do this efficiently on an electrochemical time scale. This result was initially surprising since the cobalt analog of **1** (**5**) was capable of electrocatalytically reducing O_2 , albeit with low turnover frequencies. The inability of **1** to promote the ORR is likely a consequence of its higher M(III/II) potential and thus lower overpotential for the ORR; the Co(III/II) reduction potential was -0.49 V vs $\text{Fc}^{+/0}$ (Table 2). The lesser thermodynamic driving force for metal oxidation in **1** would be anticipated to slow its reactivity with O_2 , which would generate an Fe(III)-superoxo species.

Table 2. Comparison of Electrocatalytic Parameters for Electrocatalytic O_2 Reduction by 2, 3, 4, $[Co^{II}(H_2qp1)]^{2+}$ (5), and $[Co^{II}(Hpp1)]^{2+}$ (6)^d

complex	$E_{1/2}$ for M(III/II) (V vs Fc ^{+/0})	$\eta_{\mathrm{eff}}\left(\mathrm{V}\right)$	${{TOF_{max}} \choose {(s^{-1})}}$	yield H_2O $(\%)^a$
2	-0.67	0.58	14.6	92
3	-0.56	0.42	3.3	83
3′	-0.56	0.37	3.2	81
4	-0.52	0.41	N.D.	26
5	-0.49^{c}	0.33 ^{b,c}	$0.31^{b,c}$	61 ^{b,c}
6	-0.47^{c}	$0.31^{b,c}$	$0.32^{b,c}$	$11^{b,c}$

"Percent yield calculated from RRDE measurements. ^bElectrocatalysis done with 1.0 mM catalyst and 100 mM acetate buffer (50 mM AcOH/50 mM NaOAc). ^cData from reference. ⁴¹ ^dAll data were acquired in MeCN under N₂ with 100 mM TBAPF₆ as a supporting electrolyte.

Alternatively, the more highly coordinating H_2qp1 ligand could block O_2 access to the metal center. The higher acidity of the quinolic O–H group in 1 indicates a stronger interaction between the quinol/quinolate and the iron. We do not, however, believe that this explains the lack of reactivity for 1. First, we did not see a similar lack of electrocatalytic activity for 5. Second, the ability of 1 to react with O_2 is not entirely impeded; our EPR data indicate that O_2 can oxidize 1 to an Fe(III) species.

Complexes **2** and **3** are much more active as electrocatalysts than **4**, and both of the former selectively favor the 4e⁻ pathway. Catalyst **2** can reduce O_2 with a TOF_{max} of 14.6 s⁻¹ at an η_{eff} of 0.58 V; whereas, the η_{eff} and TOF_{max} for **3** are 0.42 V and 3.3 s⁻¹, respectively. According to the more conservative RRDE measurements, the yields of water from the electrocatalytic ORR are 92% (**2**) and 83% (**3**). Relative to **5**, both Fe(II) catalysts operate at a higher overpotential but are much more active and noticeably more selective for water (Table **2**). We could not measure a reliable TOF_{max} for **4**, but the electrocatalyzed ORR instead favors H_2O_2 .

Complex 2 appears to deposit onto the electrode to a slight extent, but this appears to be much more severe for 2'. For the H_4 qp2 ligand, we hypothesize that the Fe(III) complex is less soluble than its Fe(II) analog in MeCN; this would exacerbate the deposition. With 3', however, we do not observe significant heterogeneous behavior. The absence of this phenomenon allows us to assess how the entry point into the catalytic cycle—Fe(II) vs Fe(III)—impacts the electrocatalysis of ORR. We were unable to find a similar study in the ORR literature. We find that the TOF_{max} and preference for water production are identical within error for 3 and 3' (Table 2). The rate laws are also identical, and both compounds make the transition

from an acid-dependent RDS to an acid-independent one at approximately the same buffer concentration (Figure 8). The only substantial difference between 3 and 3' is that the effective overpotential for 3' is 50 mV lower. Our results suggest that entering the catalytic cycle through the more oxidized form leads to more efficient dioxygen reduction.

We believe that the $E_{\rm cat/2}$ shifts to more negative values for the Fe(II) complex due to the coordination of O_2 prior to reduction. With the electrocatalysis observed for 3', Fe(III) is first reduced to Fe(II) at a more positive potential prior to coordination of O_2 and subsequent catalysis. With 3, however, the coordination of O_2 to the Fe(II) complex in the bulk solution occurs prior to reduction. The relevant reduction step instead corresponds to that of an Fe(III)-superoxo complex; the presence of the superoxide anion in the coordination sphere stabilizes the +3 oxidation state and renders the reduction potential more negative.

Among the Fe(II) complexes, the additional quinol in 2 confers greater activity and selectivity for water at the cost of a 0.13 V higher η_{eff} (Table 2). Comparing 3 and its phenolic analog 4, we see that using a quinol instead of a phenol improves both the activity and the selectivity for water production while having a negligible impact on the overpotential. This contrasts with what we observed for cobalt complexes with quinol- and phenol-containing ligands; with cobalt, substituting a quinol for a phenol does not significantly impact the rate of O2 reduction.41 Although the phenolic $[Co^{II}(Hpp1)]^{2+}$ (6) overwhelmingly makes H_2O_2 instead of water while operating at almost the same effective overpotential as 5, the TOF_{max} values of 5 and 6 are nearly identical (Table 2). Given that the H₄qp2 and H₂qp3 complexes with Fe(II) are much more active than the practically inert Fe(II)— H₂qp1 complex, the question remains whether these two ligands will likewise augment electrocatalytic oxygen reduction with cobalt. We are currently conducting studies to determine whether this is the case.

With other molecular electrocatalysts for the ORR, it has been observed that the selectivity for water and the rate constant for the activity both generally scale with $\eta_{\rm eff}$. $^{13,23,28,32,35-38,40,42,61}$ Higher overpotentials tend to be associated with more active catalysts that produce water instead of H₂O₂. With cobalt, the inclusion of the quinol into the ligand framework partially disrupted these scaling relationships, as evidenced by 5 preferring water and 6 favoring H₂O₂ production at nearly identical overpotentials (Table 2).41 With iron, these scaling relationships are further disrupted by the introduction of the quinol in that 3 is not only more selective for water but also more active than 4 while operating at essentially the same overpotential. Considering just the ironquinol complexes and the cobalt-containing 5, the scaling relationships seem to hold in that the electrocatalytic capabilities of 2, 3, and 5 align well with η_{eff} . Complex 2 has the higher overpotential and is both more active and more selective for water. As mentioned previously, 3' is as electrocatalytically active as 3 despite its 60 mV lower overpotential.

$$TOF = \frac{TOF_{max}}{1 + \exp\left[\frac{F}{RT}(E_{O_2/H_2O} - E_{cat/2} - \eta)\right]}$$
(9)

Figure 10 shows Tafel plots generated from eq 9 using data presented in Table 2 for catalysts which were found to be highly selective for H_2O . Here, the TOF_{max} values for each

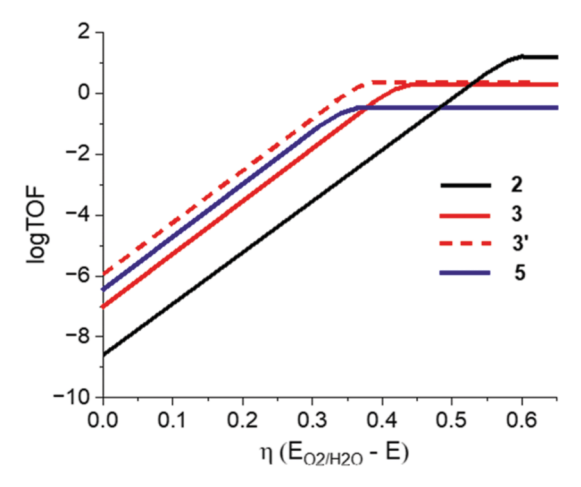


Figure 10. Tafel plots generated from TOF $_{\rm max}$ (s $^{-1}$) and $\eta_{\rm eff}$ ($E_{{\rm O}_2/{\rm H}_2{\rm O}}$ – $E_{{\rm cat}/2}$) shown in Table 2 for catalysts with high selectivity for H $_2{\rm O}$ production. Note that the x-axis represents the overpotential between the applied potential (E) and the calculated potential for O $_2$ reduction to H $_2{\rm O}$ ($E_{{\rm O}_2/{\rm H}_2{\rm O}}$). The TOF values correspond to electrocatalysis in MeCN containing 100 mM TBAPF $_6$, 400 mM acetate buffer, 6.3 mM O $_2$, and catalyst concentrations of 0.15 mM (2), 0.1 mM (3, 3'), and 1.0 mM (5).

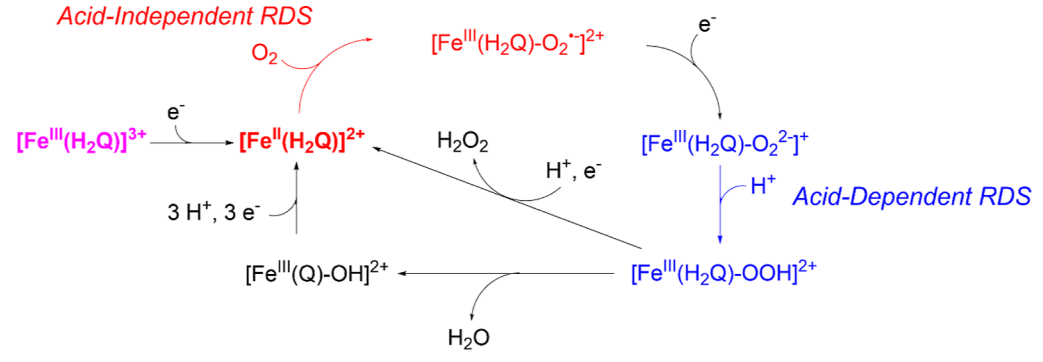
catalyst can be more clearly compared as a function of the overpotential for catalytic O_2 reduction by the electrode (η = E_{O_2/H_2O} – E). The "elbow" of each line represents the TOF generated at $\eta_{\rm eff}$ $(E_{\rm O_2/H_2O}-E_{\rm cat/2})$ for each catalyst. Although 2 produced the highest TOF_{max} this comes at a moderate cost to the overpotential. Catalysts 3, 3', and 5 yield smaller TOF_{max} values but at significantly lower η . A quantitative comparison of these catalysts can be made by examining the TOF calculated at $\eta = 0$ V (TOF₀). This value is similar to the exchange rate constant observed for heterogeneous catalysts where larger values represent greater intrinsic catalytic function. Calculated log(TOF₀) values for catalysts 2, 3, 3', and 5 were -8.5, -6.9, -5.9, and -6.4, respectively. The largest value obtained for 3' indicates this is the best catalyst of the group, producing the highest TOF at a comparative overpotential. A comparison of 3 and 3' further shows that the lower $\eta_{\rm eff}$ observed for the Fe(III) catalyst yields a 10-fold increase in TOF₀. Furthermore, based on these metrics, the performances of the quinol-containing catalysts either equal or

exceed those of the best catalysts reported in the literature, all of which are Fe(III)-porphyrin derivatives. ^{42,67} Most examples of this class have reported TOF_{max} and $\eta_{\rm eff}$ values which yield much lower calculated log(TOF₀) values ranging from -20 to -14. A notable exception was reported by Martin et al.; they found that a tetracationic substituted Fe(III) porphyrin produced TOF_{max} = 170 s⁻¹, $\eta_{\rm eff}$ = 0.54 V, and log(TOF₀) = -6.9 (MeCN, 0.1 M TBABF₄, 0.1 M AcOH/TBAA, 1 atm O₂). ⁵² These metrics are most comparable with catalysts 3, 3′, and 5; the log(TOF₀) of -5.9 for 3′ is, to the best of our knowledge, the largest such value reported for homogeneous ORR electrocatalysis.

The rate laws for the ORR catalyzed by 2, 3, and 3' are highly similar to those formulated for 5. The rate is first-order with respect to the concentrations of catalyst and O₂ (Figure 8). The dependence on the concentration of acid is more complicated in that the $k_{
m obs}$ values initially increase linearly with the concentration of buffered acid but appear to approach a plateau once a threshold concentration is reached. Such behavior was previously seen for 5 and suggests that the RDS of the catalytic mechanism changes from one that involves acid to one that does not once the acid-dependent step becomes sufficiently quick.⁴¹ We proposed that the second possible RDS corresponds to O₂ coordinating to the metal center. The transition occurs at approximately 30 mM acetate buffer for 2 and at 100 mM acetate buffer for 3, 3', and 5. The TOF_{max} values on Table 2 are obtained with 400 mM acetate buffer; under such conditions, the second RDS is operable.

Based on our electrochemical and spectroscopic data, we therefore propose that the overall mechanism for the reduction of O2 to H2O by 2 and 3 occurs via an ECEC mechanism following O2 coordination to the complexes in the bulk solution to generate Fe(III)-superoxo species that act as the active catalysts (Scheme 3). We hypothesize that the reduction of the Fe(III)-superoxo complexes to Fe(III)-peroxo species is the first E step. This reduction is then quickly followed by protonation from the buffer. The kinetic data are consistent with this C step being the RDS at low concentrations of buffered acid. The Fe(III)-OOH species made from this step are proposed to subsequently engage in rapid proton transfer and proton coupled electron transfer (PCET) reactions with the pendent quinol(s) to yield H₂O and Fe(III)-OH species. The subsequent post-RDS addition of 3e⁻ and 3H⁺ yields another equiv of H2O and regenerates the starting electrocatalysts. The H2O2 that is generated as a side-product is

Scheme 3. Proposed Mechanism of Electrocatalytic O₂ Reduction for Iron-Quinol Complexes^a



Intramolecular PCET, Major Pathway

[&]quot;Compounds 2 and 3 enter the cycle as $[Fe^{II}(H_2Q)]^{2+}$. Compounds 2' and 3' enter the cycle as $[Fe^{III}(H_2Q)]^{3+}$.

believed to result from the protonation of the Fe(III)–OOH species from the first C step. Installing a second quinol onto the ligand is proposed to decrease the amount of $\rm H_2O_2$ produced by making the intramolecular PCET reactions that lead to water production faster.

We propose that 2' and 3' follow the same mechanistic cycle with the same possible RDS as their Fe(II) analogs. The Fe(III) compounds differ in how they enter the catalytic pathway. We propose that the initial steps for 2' and 3' involve reduction of the metal center followed by dioxygen binding.

In the absence of a current, we may be able to trap the Fe(III)-OH intermediates formed from 3. When the reaction between 3 and O_2 is studied without a current and acetate buffer, we observe m/z peaks consistent with $[Fe^{III}(Hqp3)-(OH)]^+$, $[Fe^{III}(Hqp3)]^{2+}$, and $[Fe^{III}(qp3)]^{2+}$ (Figure S48). The presence of the latter two species suggests that the Fe(II) and quinol are sufficiently good terminal sources of electrons and protons, respectively, to stoichiometrically activate O_2 . We do not observe an Fe(III)-OH species for 2. That we instead see $[Fe^{III}(H_2qp2)]^+$ may suggest that the second quinol transfers a proton to the hydroxide to yield an $Fe(III)-OH_2$ species and quinolate; the quinolate then displaces the more labile water from the metal center.

The quinols in the iron complexes lower the free energy barriers for both possible RDS. With lower concentrations of acid, the rate constant for intermolecular H^+ transfer (inter- k_{H^+}) is much higher for 2 than for 3 and 3' (Table 3). This can

Table 3. Estimated Rate Constants for O_2 Reduction Catalyzed by Iron and Cobalt Complexes with Quinolic and Phenolic Ligands^f

com	plex	inter- $k_{H^{+}} (M^{-1} s^{-1})^{a}$	intra- k_{H^+} $(s^{-1})^b$	$k_{\rm O_2} ({\rm M}^{-1} {\rm s}^{-1})^c$
2	2	130	1.2	2200
3	3	34	0.021	480
3	3′	30	0.048	470
4	ŀ	N.D.	N.D.	N.D.
5	;	8.1 ^d	0.052^{d}	48 ^d
6	6	5.6 ^d	0.047^{d}	110 ^{d,e}

"Rate constant for intermolecular proton transfer from the buffer to the catalyst. Estimated using the slopes of the buffer-dependent portions of the $k_{\rm obs}$ vs [buffer] plots (Figure 8B,E,H). $[{\rm O_2}]=6.3$ mM. Rate constant for intramolecular proton transfer. Estimated using the intercepts of the buffer-dependent $k_{\rm obs}$ vs [buffer] plots (Figure 8B,E,H). $[{\rm O_2}]=6.3$ mM. Rate constant for ${\rm O_2}$ binding. Estimated using the slopes of $[{\rm O_2}]$ -dependent plots (Figure 8A,D,G) with 400 mM acetate buffer. Data from reference. Estimated from the peak $k_{\rm obs}$ for the acid-independent portion of the $k_{\rm obs}$ vs [buffer] plot. $k_{\rm O_2}=k_{\rm obs}/[{\rm O_2}]$, with $[{\rm O_2}]=6.3$ mM. All data were acquired in MeCN with 100 mM TBAPF₆ as a supporting electrolyte.

be rationalized by the second quinol in **2** serving as an additional proton relay group; similar effects have been documented for other small molecule electrocatalysts for the ORR. 21,30,39,68 The additional quinol in **2** also hastens intramolecular H⁺ transfer—which enables some electrocatalytic O_2 reduction in the absence of a buffered proton source—as evidenced by the higher intra- $k_{\rm H}$ rate constant (Table 3). With **5** and **6**, we likewise found nonzero intercepts and evidence of intramolecular H⁺ transfer. The calculated intra- $k_{\rm H}$ for the cobalt complexes are approximately equal to those of **3** and **3** and much less than that for **2**; this is consistent with the H₄qp2 being able to provide more protons.

The rate constants for O_2 binding (k_{O_2}) are much higher for the iron complexes than for their cobalt analogs, and the second quinol in 2 hastens this step as well (Table 3). With 5 and 6, the quinol-for-phenol substitution appears to slow O_2 binding, with the caveats that the k_{O_2} for 6 was calculated from the plateau of the $k_{\rm obs}$ vs [buffer] plot as opposed to a $k_{\rm obs}$ vs $[O_2]$ plot and that these values were not measured under acidindependent conditions. The opposite effect is observed for 3, 3', and 4; with the iron complexes, the phenolic 4 is a far inferior electrocatalyst. Less efficient O_2 binding likely contributes to the lack of activity, but we could not estimate rate constants from the available data to fully support this hypothesis. We believe that the faster O_2 binding for 2 is correlated to the more negative Fe(III/II) reduction potential, but the additional quinol could also hydrogen bond to and stabilize a metal-bound O_2 .

CONCLUSIONS

Our results show that iron complexes with quinol-containing ligands can be effective electrocatalysts for dioxygen reduction but that this activity is highly dependent on the coordination environment. The activity is lost when the Fe(III/II) reduction potential is not sufficiently negative. Installing a second quinol onto the ligand improves both the selectivity for four-electron reduction of O2 to water and the overall activity of the electrocatalyst while modestly raising the effective overpotential. The additional quinol appears to make both intramolecular proton transfer and dioxygen binding more efficient. The catalysts differ from others that have been previously reported in that they can enter the mechanistic cycle with two different metal oxidation states. With a previous cobalt system, the electrocatalysis with a quinol ligand and its phenolic analog had approximately equal activities and overpotentials but greatly different product selectivities. The quinols in the iron complexes reported here also enhance the catalytic activity in addition to favoring more water production.

ASSOCIATED CONTENT

Solution Supporting Information

The Supporting Information is available free of charge at https://pubs.acs.org/doi/10.1021/acs.inorgchem.4c01977.

Characterization and electrocatalytic data for all iron complexes (PDF)

AUTHOR INFORMATION

Corresponding Authors

Byron H. Farnum – Department of Chemistry and Biochemistry, Auburn University, Auburn, Alabama 36849, United States; Email: farnum@auburn.edu

Christian R. Goldsmith – Department of Chemistry and Biochemistry, Auburn University, Auburn, Alabama 36849, United States; ⊚ orcid.org/0000-0001-7293-1267; Email: crgoldsmith@auburn.edu

Authors

Segun V. Obisesan – Department of Chemistry and Biochemistry, Auburn University, Auburn, Alabama 36849, United States

Maksuda Parvin – Department of Chemistry and Biochemistry, Auburn University, Auburn, Alabama 36849, United States

Matthew Tao — Department of Chemistry and Biochemistry, Auburn University, Auburn, Alabama 36849, United States Eric Ramos — Department of Chemistry and Biochemistry, Auburn University, Auburn, Alabama 36849, United States Alexander C. Saunders — Department of Chemistry and Biochemistry, Auburn University, Auburn, Alabama 36849, United States

Complete contact information is available at: https://pubs.acs.org/10.1021/acs.inorgchem.4c01977

Notes

The authors declare no competing financial interest.

ACKNOWLEDGMENTS

The research described here was financially supported by Auburn University and a grant from the National Science Foundation (NSF-CHE-1954336). E.R. also acknowledges summer support from the Auburn University CASE REU program (NSF-1950304).

REFERENCES

- (1) Campos-Martin, J. M.; Blanco-Brieva, G.; Fierro, J. L. G. Hydrogen Peroxide Synthesis: An Outlook beyond the Anthraquinone Process. *Angew. Chem., Int. Ed.* **2006**, 45 (42), 6962–6984.
- (2) Solomon, E. I.; Stahl, S. S. Introduction: Oxygen Reduction and Activation in Catalysis. *Chem. Rev.* **2018**, *118* (5), 2299–2301.
- (3) Shao, M.; Chang, Q.; Dodelet, J.-P.; Chenitz, R. Recent Advances in Electrocatalysts for Oxygen Reduction Reaction. *Chem. Rev.* **2016**, *116* (6), 3594–3657.
- (4) Collman, J. P.; Boulatov, R.; Sunderland, C. J.; Fu, L. Functional Analogues of Cytochrome c Oxidase, Myoglobin, and Hemoglobin. *Chem. Rev.* **2004**, *104* (2), 561–588.
- (5) Rittle, J.; Green, M. T. Cytochrome P450 Compound I: Capture, Characterization, and C-H Bond Activation Kinetics. *Science* **2010**, 330 (6006), 933–937.
- (6) Ogliaro, F.; de Visser, S. P.; Cohen, S.; Sharma, P. K.; Shaik, S. Searching for the Second Oxidant in the Catalytic Cycle of Cytochrome P450: A Theoretical Investigation of the Iron(III)-Hydroperoxo Species and Its Epoxidation Pathways. *J. Am. Chem. Soc.* **2002**, *124* (11), 2806–2817.
- (7) Yoshikawa, S.; Shimada, A. Reaction Mechanism of Cytochrome c Oxidase. *Chem. Rev.* **2015**, *115* (4), 1936–1989.
- (8) Poulos, T. L. Heme Enzyme Structure and Function. *Chem. Rev.* **2014**, *114* (7), 3919–3962.
- (9) Abu-Omar, M. M.; Loaiza, A.; Hontzeas, N. Reaction Mechanisms of Mononuclear Non-Heme Iron Oxygenases. *Chem. Rev.* 2005, 105 (6), 2227–2252.
- (10) Chlistunoff, J.; Sansiñena, J.-M. Effects of Axial Coordination of the Metal Center on the Activity of Iron Tetraphenylporphyrin as a Nonprecious Catalyst for Oxygen Reduction. *J. Phys. Chem. C* **2014**, *118* (33), 19139–19149.
- (11) Ohta, T.; Nagaraju, P.; Liu, J.-G.; Ogura, T.; Naruta, Y. The Secondary Coordination Sphere and Axial Ligand Effects on Oxygen Reduction Reaction by Iron Porphyrins: a DFT Computational Study. *J. Biol. Inorg. Chem.* **2016**, *21* (5–6), 745–755.
- (12) Kobayashi, N.; Nishiyama, Y. Catalytic Electroreduction of Molecular Oxygen Using Iron or Cobalt 4,4',4",4""-Tetracarboxyphthalocyanine. J. Phys. Chem. 1985, 89 (7), 1167–1170.
- (13) Costentin, C.; Dridi, H.; Savéant, J.-M. Molecular Catalysis of O₂ Reduction by Iron Porphyrins in Water: Heterogeneous versus Homogeneous Pathways. *J. Am. Chem. Soc.* **2015**, *137* (42), 13535–13544.
- (14) Wang, Y.-H.; Schneider, P. E.; Goldsmith, Z. K.; Mondal, B.; Hammes-Schiffer, S.; Stahl, S. S. Brønsted Acid Scaling Relationships Enable Control Over Product Selectivity from O_2 Reduction with a

- Mononuclear Cobalt Porphyrin Catalyst. ACS Cent. Sci. 2019, 5 (6), 1024–1034.
- (15) Martin, D. J.; Mayer, J. M. Oriented Electrostatic Effects on O_2 and CO_2 Reduction by a Polycationic Iron Porphyrin. *J. Am. Chem. Soc.* **2021**, *143* (30), 11423–11434.
- (16) Brezny, A. C.; Johnson, S. I.; Raugei, S.; Mayer, J. M. Selectivity-Determining Steps in O₂ Reduction Catalyzed by Iron-(tetramesitylporphyrin). *J. Am. Chem. Soc.* **2020**, 142 (9), 4108–4113.
- (17) Rigsby, M. L.; Wasylenko, D. J.; Pegis, M. L.; Mayer, J. M. Medium Effects Are as Important as Catalyst Design for Selectivity in Electrocatalytic Oxygen Reduction by Iron-Porphyrin Complexes. *J. Am. Chem. Soc.* **2015**, *137* (13), 4296–4299.
- (18) Singha, A.; Mondal, A.; Nayek, A.; Dey, S. G.; Dey, A. Oxygen Reduction by Iron Porphyrins with Covalently Attached Pendent Phenol and Quinol. *J. Am. Chem. Soc.* **2020**, *142* (52), 21810–21828.
- (19) Carver, C. T.; Matson, B. D.; Mayer, J. M. Electrocatalytic Oxygen Reduction by Iron Tetra-arylporphyrins Bearing Pendant Proton Relays. *J. Am. Chem. Soc.* **2012**, *134* (12), 5444–5447.
- (20) Dong, Y.; Lv, X.; Sun, Y.; Zhao, Q.; Lei, H.; Wu, F.; Zhang, T.; Xue, Z.; Cao, R.; Qiu, F.; Xue, S. Electrocatalytic Oxygen Reduction Reaction of Peripheral Functionalized Cobalt Porphyrins(2.1.2.1). *Inorg. Chem.* **2024**, *63* (11), 4797–4801.
- (21) Ghatak, A.; Samanta, S.; Nayek, A.; Mukherjee, S.; Dey, S. G.; Dey, A. Second-Sphere Hydrogen-Bond Donors and Acceptors Affect the Rate and Selectivity of Electrochemical Oxygen Reduction by Iron Porphyrins Differently. *Inorg. Chem.* **2022**, *61* (33), 12931–12947.
- (22) Gasteiger, H. A.; Kocha, S. S.; Sompalli, B.; Wagner, F. T. Activity Benchmarks and Requirements for Pt, Pt-Alloy, and Non-Pt Oxygen Reduction Catalysts for PEMFCs. *Appl. Catal., B* **2005**, *56* (1–2), 9–35.
- (23) Wang, Y.-H.; Mondal, B.; Stahl, S. S. Molecular Cobalt Catalysts for O_2 Reduction to H_2O_2 : Benchmarking Catalyst Performance via Rate-Overpotential Correlations. *ACS Catal.* **2020**, 10 (20), 12031–12039.
- (24) Kobayashi, N.; Nevin, W. A. Electrocatalytic Reduction of Oxygen Using Water-Soluble Iron and Cobalt Phthalocyanines and Porphyrins. *Appl. Organomet. Chem.* **1996**, *10* (8), 579–590.
- (25) Guo, H.-B.; Wang, Y.-N.; Guo, K.; Lei, H.-T.; Liang, Z.-Z.; Zhang, X.-P.; Cao, R. A Co Porphyrin with Electron-Withdrawing and Hydrophilic Substituents for Improved Electrocatalytic Oxygen Reduction. *J. Electrochem.* 2022, 28 (9), 2214002.
- (26) Liu, T.; Qin, H.; Xu, Y.; Peng, X.; Zhang, W.; Cao, R. Steric Effects on the Oxygen Reduction Reaction with Cobalt Porphyrin Atropisomers. ACS Catal. 2024, 14 (9), 6644–6649.
- (27) Meng, J.; Qin, H.; Lei, H.; Li, X.; Fan, J.; Zhang, W.; Apfel, U.-P.; Cao, R. Adapting Synthetic Models of Heme/Cu Sites to Energy-Efficient Electrocatalytic Oxygen Reduction Reaction. *Angew. Chem., Int. Ed.* **2023**, 62 (51), No. e202312255.
- (28) Wang, Y.-H.; Pegis, M. L.; Mayer, J. M.; Stahl, S. S. Molecular Cobalt Catalysts for O₂ Reduction: Low-Overpotential Production of H₂O₂ and Comparison with Iron-Based Catalysts. *J. Am. Chem. Soc.* **2017**, 139 (46), 16458–16461.
- (29) Nichols, A. W.; Kuehner, J. S.; Huffman, B. L.; Miedaner, P. R.; Dickie, D. A.; Machan, C. W. Reduction of Dioxygen to Water by a $Co(N_2O_2)$ Complex with a 2,2'-Bipyridine Backbone. *Chem. Commun.* **2021**, 57 (4), 516–519.
- (30) Nichols, A. W.; Cook, E. N.; Gan, Y. J.; Miedaner, P. R.; Dressel, J. M.; Dickie, D. A.; Shafaat, H. S.; Machan, C. W. Pendent Relay Enhances H₂O₂ Selectivity during Dioxygen Reduction Mediated by Bipyridine-Based Co-N₂O₂ Complexes. *J. Am. Chem. Soc.* **2021**, *143* (33), 13065–13073.
- (31) Wang, Y.-H.; Goldsmith, Z. K.; Schneider, P. E.; Anson, C. W.; Gerken, J. B.; Ghosh, S.; Hammes-Schiffer, S.; Stahl, S. S. Kinetic and Mechanistic Characterization of Low-Overpotential, H₂O₂-Selective Reduction of O₂ Catalyzed by N₂O₂-Ligated Cobalt Complexes. *J. Am. Chem. Soc.* **2018**, *140* (34), 10890–10899.
- (32) Cook, E. N.; Dickie, D. A.; Machan, C. W. Catalytic Reduction of Dioxygen to Water by a Bioinspired Non-Heme Iron Complex via a 2+2 Mechanism. *J. Am. Chem. Soc.* **2021**, *143* (40), 16411–16418.

- (33) Cook, E. N.; Hooe, S. L.; Dickie, D. A.; Machan, C. W. Homogeneous Catalytic Reduction of O₂ to H₂O by a Terpyridine-Based FeN₃O Complex. *Inorg. Chem.* **2022**, *61* (22), 8387–8392.
- (34) Machan, C. W. Advances in the Molecular Catalysis of Dioxygen Reduction. ACS Catal. 2020, 10 (4), 2640–2655.
- (35) Pegis, M. L.; Wise, C. F.; Martin, D. J.; Mayer, J. M. Oxygen Reduction by Homogeneous Molecular Catalysts and Electrocatalysts. *Chem. Rev.* **2018**, *118* (5), 2340–2391.
- (36) Wang, L.; Gennari, M.; Cantú Reinhard, F. G.; Gutiérrez, J.; Morozan, A.; Philouze, C.; Demeshko, S.; Artero, V.; Meyer, F.; de Visser, S. P.; Duboc, C. A Non-Heme Diiron Complex for (Electro)catalytic Reduction of Dioxygen: Tuning the Selectivity through Electron Delivery. J. Am. Chem. Soc. 2019, 141 (20), 8244–8253.
- (37) Passard, G.; Ullman, A. M.; Brodsky, C. N.; Nocera, D. G. Oxygen Reduction Catalysis at a Dicobalt Center: The Relationship of Faradaic Efficiency to Overpotential. *J. Am. Chem. Soc.* **2016**, *138* (9), 2925–2928.
- (38) Anson, C. W.; Stahl, S. S. Cooperative Electrocatalytic O_2 Reduction Involving Co(salophen) with p-Hydroquinone as an Electron-Proton Transfer Mediator. J. Am. Chem. Soc. **2017**, 139 (51), 18472–18475.
- (39) Cook, E. N.; Courter, I. M.; Dickie, D. A.; Machan, C. W. Controlling Product Selectivity during Dioxygen Reduction with Mn Complexes Using Pendent Proton Donor Relays and Added Base. *Chem. Sci.* **2024**, *15* (12), 4478–4488.
- (40) Hooe, S. L.; Rheingold, A. L.; Machan, C. W. Electrocatalytic Reduction of Dioxygen to Hydrogen Peroxide by a Molecular Manganese Complex with a Bipyridine-Containing Schiff Base Ligand. *J. Am. Chem. Soc.* **2018**, *140* (9), 3232–3241.
- (41) Obisesan, S. V.; Rose, C.; Farnum, B. H.; Goldsmith, C. R. Co(II) Complex with a Covalently Attached Pendent Quinol Selectively Reduces O₂ to H₂O. *J. Am. Chem. Soc.* **2022**, *144* (50), 22826–22830.
- (42) Pegis, M. L.; McKeown, B. A.; Kumar, N.; Lang, K.; Wasylenko, D. J.; Zhang, X. P.; Raugei, S.; Mayer, J. M. Homogenous Electrocatalytic Oxygen Reduction Rates Correlate with Reaction Overpotential in Acidic Organic Solutions. *ACS Cent. Sci.* **2016**, 2 (11), 850–856.
- (43) Dinda, S.; Siddiqui, A. I.; Behera, S.; Mondal, B. Demystifying the Role of Covalently Attached Electron-Proton Transfer Mediator in Oxygen Reduction Reaction Catalyst. *ACS Catal.* **2023**, *13* (19), 12643–12647.
- (44) Yu, M.; Ambrose, S. L.; Whaley, Z. L.; Fan, S.; Gorden, J. D.; Beyers, R. J.; Schwartz, D. D.; Goldsmith, C. R. A Mononuclear Manganese(II) Complex Demonstrates a Strategy to Simultaneously Image and Treat Oxidative Stress. J. Am. Chem. Soc. 2014, 136, 12836—12839.
- (45) Yu, M.; Ward, M. B.; Franke, A.; Ambrose, S. L.; Whaley, Z. L.; Bradford, T. M.; Gorden, J. D.; Beyers, R. J.; Cattley, R. C.; Ivanović-Burmazović, I.; Schwartz, D. D.; Goldsmith, C. R. Adding a Second Quinol to a Redox-Responsive MRI Contrast Agent Improves Its Relaxivity Response to H₂O₂. *Inorg. Chem.* **2017**, *56* (5), 2812–2826.
- (46) Connelly, N. G.; Geiger, W. E. Chemical Redox Agents for Organometallic Chemistry. *Chem. Rev.* 1996, 96 (2), 877–910.
- (47) Li, Q.; Batchelor-McAuley, C.; Lawrence, N. S.; Hartshorne, R. S.; Compton, R. G. Anomalous Solubility of Oxygen in Acetonitrile/Water Mixture Containing Tetra-n-butylammonium Perchlorate Supporting Electrolyte; the Solubility and Diffusion Coefficient of Oxygen in Anhydrous Acetonitrile and Aqueous Mixtures. J. Electroanal. Chem. 2013, 688, 328–335.
- (48) Zhou, R.; Zheng, Y.; Jaroniec, M.; Qiao, S.-Z. Determination of the Electron Transfer Number for the Oxygen Reduction Reaction: From Theory to Experiment. *ACS Catal.* **2016**, *6* (7), 4720–4728.
- (49) Lee, Y.; Park, G. Y.; Lucas, H. R.; Vajda, P. L.; Kamaraj, K.; Vance, M. A.; Milligan, A. E.; Woertink, J. S.; Siegler, M. A.; Narducci Sarjeant, A. A.; Zakharov, L. N.; Rheingold, A. L.; Solomon, E. I.; Karlin, K. D. Copper(I)/O₂ Chemistry with Imidazole Containing

- Tripodal Tetradentate Ligands Leading to μ -1,2-Peroxo-Dicopper(II) Species. *Inorg. Chem.* **2009**, 48 (23), 11297–11309.
- (50) Costentin, C.; Drouet, S.; Robert, M.; Savéant, J.-M. Turnover Numbers, Turnover Frequencies, and Overpotential in Molecular Catalysis of Electrochemical Reactions. Cyclic Voltammetry and Preparative-Scale Electrolysis. *J. Am. Chem. Soc.* **2012**, *134* (27), 11235–11242.
- (51) Wang, V. C.-C.; Johnson, B. A. Interpreting the Electrocatalytic Voltammetry of Homogeneous Catalysts by the Foot of the Wave Analysis and Its Wider Implications. *ACS Catal.* **2019**, *9* (8), 7109–7123
- (52) Martin, D. J.; Mercado, B. Q.; Mayer, J. M. Combining Scaling Relationships Overcomes Rate versus Overpotential Trade-Offs in O₂ Molecular Electrocatalysis. *Sci. Adv.* **2020**, *6* (11), No. eaaz3318.
- (53) Kütt, A.; Leito, I.; Kaljurand, I.; Sooväli, L.; Vlasov, V. M.; Yagupolskii, L. M.; Koppel, I. A. A Comprehensive Self-Consistent Spectrophotometric Acidity Scale of Neutral Brønsted Acids in Acetonitrile. *J. Org. Chem.* **2006**, *71* (7), 2829–2838.
- (54) Moore, J. L.; Oppelt, J.; Senft, L.; Franke, A.; Scheitler, A.; Dukes, M. W.; Alix, H. B.; Saunders, A. C.; Karbalaei, S.; Schwartz, D. D.; Ivanović-Burmazović, I.; Goldsmith, C. R. Diquinol Functionality Boosts the Superoxide Dismutase Mimicry of a Zn(II) Complex with a Redox-Active Ligand while Maintaining Catalyst Stability and Enhanced Activity in Phosphate Solution. *Inorg. Chem.* **2022**, *61* (49), 19983–19997.
- (55) Ward, M. B.; Scheitler, A.; Yu, M.; Senft, L.; Zillmann, A. S.; Gorden, J. D.; Schwartz, D. D.; Ivanović-Burmazović, I.; Goldsmith, C. R. Superoxide Dismutase Activity Enabled by a Redox-Active Ligand rather than Metal. *Nat. Chem.* **2018**, *10* (12), 1207–1212.
- (56) Karbalaei, S.; Franke, A.; Jordan, A.; Rose, C.; Pokkuluri, P. R.; Beyers, R. J.; Zahl, A.; Ivanović-Burmazović, I.; Goldsmith, C. R. A Highly Water- and Air-Stable Iron-Containing MRI Contrast Agent Sensor for H₂O₂. *Chem.—Eur. J.* **2022**, 28, No. e202201179.
- (57) Karbalaei, S.; Knecht, E.; Franke, A.; Zahl, A.; Saunders, A. C.; Pokkuluri, P. R.; Beyers, R. J.; Ivanović-Burmazović, I.; Goldsmith, C. R. A Macrocyclic Ligand Framework That Improves Both the Stability and T₁-Weighted MRI Response of Quinol-Containing H₂O₂ Sensors. *Inorg. Chem.* **2021**, *60* (12), 8368–8379.
- (58) Galicia, M.; González, F. J. Electrochemical Oxidation of Tetrabutylammonium Salts of Aliphatic Carboxylic Acids in Acetonitrile. *J. Electrochem. Soc.* **2002**, *149* (3), D46.
- (59) Hooe, S. L.; Cook, E. N.; Reid, A. G.; Machan, C. W. Non-Covalent Assembly of Proton Donors and *p*-Benzoquinone Anions for Co-Electrocatalytic Reduction of Dioxygen. *Chem. Sci.* **2021**, *12* (28), 9733–9741.
- (60) Astudillo, P. D.; Tiburcio, J.; González, F. J. The Role of Acids and Bases on the Electrochemical Oxidation of Hydroquinone: Hydrogen Bonding Interactions in Acetonitrile. *J. Electroanal. Chem.* **2007**, *604* (1), 57–64.
- (61) Costentin, C.; Savéant, J.-M. Towards an Intelligent Design of Molecular Electrocatalysts. *Nat. Rev. Chem.* **2017**, *1* (11), 0087.
- (62) Cotton, F. A.; Wilkinson, G. Advanced Inorganic Chemistry; John Wiley & Sons, 1988.
- (63) Bordwell, F. G.; Cheng, J.-P. Substituent Effects on the Stabilities of Phenoxyl Radicals and the Acidities of Phenoxyl Radical Cations. J. Am. Chem. Soc. 1991, 113 (5), 1736–1743.
- (64) Baes, C. F.; Mesmer, R. E. Hydrolysis of Cations; Krieger Publishing Company, 1976.
- (65) Jackson, V. E.; Felmy, A. R.; Dixon, D. A. Prediction of the pK_a's of Aqueous Metal Ion +2 Complexes. *J. Phys. Chem. A* **2015**, 119 (12), 2926–2939.
- (66) Senft, L.; Moore, J. L.; Franke, A.; Fisher, K. R.; Scheitler, A.; Zahl, A.; Puchta, R.; Fehn, D.; Ison, S.; Sader, S.; Ivanović-Burmazović, I.; Goldsmith, C. R. Quinol-Containing Ligands Enable High Superoxide Dismutase Activity by Modulating Coordination Number, Charge, Oxidation States and Stability of Manganese Complexes throughout Redox Cycling. *Chem. Sci.* **2021**, *12* (31), 10483–10500.

- (67) Bhunia, S.; Ghatak, A.; Rana, A.; Dey, A. Amine Groups in the Second Sphere of Iron Porphyrins Allow for Higher and Selective 4e⁻/4H⁺ Oxygen Reduction Rates at Lower Overpotentials. *J. Am. Chem. Soc.* **2023**, *145* (6), 3812–3825.
- (68) Rakowski Dubois, M.; Dubois, D. L. Development of Molecular Electrocatalysts for CO₂ Reduction and H₂ Production/Oxidation. *Acc. Chem. Res.* **2009**, *42* (12), 1974–1982.